Helmholtz-Zentrum Dresden-Rossendorf (HZDR)

HELMHOLTZ ZENTRUM
DRESDEN ROSSENDORF

Electron microprobe petrochronology ofzite-bearing garnet micaschists in the Oetztal-Stubai Complex (Alpeiner Valley, Stubai)

Schulz, B.; Krause, J.; Zimmermann, R.;

Originally published:

November 2019

Swiss Journal of Geosciences 112(2019)2-3, 597-617

DOI: https://doi.org/10.1007/s00015-019-00351-4

Perma-Link to Publication Repository of HZDR:

https://www.hzdr.de/publications/Publ-24481

Release of the secondary publication
on the basis of the German Copyright Law § 38 Section 4.

Version 21-11-2016 submitted version

Crystallisation of Permo-Triassic monazite in the pre-Alpine Oetztal-Stubai Complex (Alpeiner Valley, Stubai, Eastern Alps)

Bernhard SCHULZ [1)*)] & Robert ZIMMERMANN [2]

[1] TU Bergakademie Freiberg, Institute of Mineralogy, Department of Economic Geology and Petrology, Brennhausgasse 14, D-09599 Freiberg/Saxony, Germany

[2] Helmholtz-Zentrum Dresden-Rossendorf, Helmholtz Institute Freiberg for Resource Technology, Division of Exploration, Halsbrücker Straße 34, D-09599 Freiberg/Saxony, Germany

*Corresponding author: Bernhard.Schulz@mineral.tu-freiberg.de

*Corresponding author:
Bernhard Schulz
TU Bergakademie Freiberg, Institut für Mineralogie, Professur für Lagerstättenkunde und Petrologie, Brennhausgasse 14, D-09599 Freiberg/Sachsen, Deutschland
E-Mail: Bernhard.Schulz@mineral.tu-freiberg.de, Tel: +49 3731 39 2668

Keywords: monazite, garnet metapelites, amphibolites, geothermobarometry, Permian, Austroalpine basement

Abstract

The Alpeiner amphibolite unit in the Stubai region is the eastern succession of the Central Metabasite Zone (CMBZ) in the Austroalpine Oetztal-Stubai-Complex (OSC). In the Alpeiner Valley, amphibolites and biotite-hornblende gneisses are alternating with metapelites and metapsammites. Garnet in metapelite assemblages display growth zonations with spessartine- and grossular-rich cores and pyrope-rich rims. Geothermobarometry signals a prograde metamorphism with amphibolite-facies peak conditions at ~ 12 kbar and ~ 680 °C. The post P_{max} path with a decompression to 4 kbar and 660 - 600 °C was estimated by geothermobarometry involving zoned Ca-amphiboles in retrogressed amphibolitized eclogites. This P-T evolution is similar to the Variscan P-T paths known from the central Oetztal and Sellrain regions. Electron microprobe Th-U-Pb monazite dating in the metapelites yielded two distinct maxima at ages around 270 Ma and 220 Ma. In detail, Carboniferous and Permian isochrone ages at 304 ± 26 Ma, 272 ± 16 Ma and 269 ± 13 Ma, but also Triassic isochrones at 209 ± 17 Ma can be extracted from 3 samples. Monazite corona microstructures suggest a decomposition during decreasing temperature. In contrast, clusters of small monazite within allanite signal a re-crystallization. This points to a complex retrograde evolution when the P-T path approached low pressures. No Permian pegmatites and no accompanying distinct low pressure high temperature metamorphic event have yet been reported from the Stubai region. Therefore the monazite age data in combination to the P-T path provide petrological arguments for a Permian-to-Triassic metamorphic event. The new data from the Stubai basement indicates that this event, known from other Austroalpine basement areas was not restricted to the pegmatite-bearing zones. This Permian-to-Triassic thermal evolution with monazite crystallization appears during the decompression after a Carboniferous continental collision with an eclogite to amphibolite-facies main metamorphism.

1. Introduction

A major part of the Eastern Alps is composed of basement units with a polymetamorphic history. The pre-Alpine Ordovician-Silurian, Carboniferous and Permian events, and the Alpine Cretaceous and Tertiary metamorphism have been reported from various parts (Frey et al., 1999). The Austroalpine Oetztal-Stubai Complex (OSC) is located in the Central Alps (Frisch et al., 2000;

59 Egglseder and Fügenschuh, 2013). It is one of the classical areas of polymetamorphism in the
60 Alps (Purtscheller, 1978; Thöni, 1999). Various isotopic dating methods have been applied there.
61 An Ordovician high-temperature anatectic event was reported from the Winnebach, Verpeil and
62 Gaisloch migmatites (Klötzli-Chowanetz et al., 1997; Neubauer et al., 1999; Hoinkes et al., 1999;
63 Söllner, 2001; Thöny et al., 2008). Eclogite-facies conditions were locally attained during the
64 Variscan (Devonian-Carboniferous) metamorphism (Mogessi et al., 1985; Mogessi and
65 Purtscheller, 1986; Miller and Thöni, 1995; Rode et al., 2012). The Variscan metamorphic overprint
66 led to kyanite, sillimanite and andalusite mineral zones (Fig. 1) of which boundaries cut across and
67 postdate the large-scale Schlingen structures of the regional foliation (Purtscheller, 1978). Towards
68 the South, an increasing grade of the Early-Alpine (Cretaceous) overprint has been described
69 (Thöni, 1981; 1983; Hoinkes et al., 1991; 1999; Hoinkes and Thöni, 1993; Thöni, 1999). This is
70 obvious from Variscan-to-Alpine K-Ar and Rb-Sr "mixed ages" of mica, changing to Cretaceous
71 ages towards the SE. The successive occurrence of chloritoid and then staurolite towards the
72 Schneeberger Zug and the Texel Complex, accompanied by distinct growth zones in garnet
73 porphyroblasts (Frank et al., 1987; Tropper and Recheis, 2003) are also assigned to this Early
74 Alpine overprint. The Late Alpine (Tertiary) events with South Alpine indenter and lateral extrusion
75 led to faults and shear zones which reframe and dissect the OSC. The main tectonic lines are the
76 sinistral Inntal fault zone to the North, the Brenner normal fault zone to the East, the Schneeberg
77 fault zone and Vinschgau shear zone to the South, the Schlinig zone to the West and the Engadine
78 line to the Northwest (Ratschbacher et al., 1991; Frisch et al., 2000; Schmid et al., 2004).
79
80 Within this frame, Permian mica ages were formerly interpreted as Carboniferous - Cretaceous
81 ”mixing ages” (Thöni, 1981). However, these days the Permian magmatic and metamorphic ages
82 which are known from various parts of the Austroalpine basement are interpreted to express a
83 distinct geodynamic event (Schuster et al., 2001; Marotta and Spalla, 2007; Schuster and Stüwe,
84 2008). The Permian event has been explained by westward propagation of the Meliata ocean in
85 the course of a post-collisional extension of the Variscan orogen. Extensional fabrics and
86 decompression melting (granites and pegmatites) are discussed as indicators for this HT/LP
87 metamorphism (Schuster and Stüwe, 2008).

In this context, the OSC represents a difficult situation for the resolution of the thermal events by age dating. Dependent on metamorphic grade and P-T paths, Rb-Sr, K-Ar and Ar-Ar methods can provide at best the age of maximal pressure and further ages on the cooling history of the latest metamorphic event. Methods based on U-Pb in zircon mostly fail, as the corresponding closure temperature and formation temperatures have not been achieved during amphibolite-facies and eclogite-facies metamorphism. Other methods as Sm-Nd in metamorphic garnet are difficult in specific applications and rarely available. In this frame, the electron microprobe (EMP) Th-U-Pb monazite dating in metapelites appears as promising. Here, we report corresponding data from the Alpeiner Valley in the OSC. The monazite ages and the P-T evolution in this part of the Austroalpine basement provide a link between the domains with Variscan metamorphism and the domains where the Permian-to-Triassic event is manifested by numerous pegmatite intrusions.

2. Geological setting and petrography

In the Alpeiner Valley around the Franz-Senn-Hütte in the NE part of the OSC, a succession from metapsammites and metapelites in the southern part, to an amphibolite dominated northern part of a Wechselserie are observed. Metagranitoids occur within this sequence (Fig. 2). Previous regional petrographic and tectonic studies (Hammer, 1929; Purtscheller, 1978; Schulz, 1994; Rode et al., 2012; Egglseder and Fügenschuh, 2013) cover the NE part of the OSC, but are lacking details from the Alpeiner Valley.

The Alpeiner metabasites are mostly amphibolites and biotite hornblende gneisses and form the eastern succession of the Central Metabasite Zone (CMBZ) of the OSC. Protoliths of the CMBZ are gabbros and basalts with MORB-chemistry (Mogessie et al., 1985) and Early Cambrian ages (Miller and Thöni, 1995), emplaced in a back-arc setting. The CMBZ is subdivided from N to S into five zones (Purtscheller, 1978): (1) Roughly foliated amphibolite with layers and lenses of eclogite and rare peridotite, (2) Dark, garnet-bearing amphibolites, (3) Alumosilicate gneisses (4) Wechselserie (5) Southern eclogite zone. The Alpeiner metabasites are alternating with metapelites to metapsammites and therefore have been assigned to the Wechselserie

(Purtscheller, 1978). Lenses of retrogressed eclogites and calc-silicate-gneisses are interbedded within the succession in the northern part (Figs 2; S1).

The metapelitic and -psammitic rocks within the study area are composed of quartzites and staurolite bearing micaschists and paragneisses. In the northern part, micaschists form lenses within the ”Wechselserie”, often not extending more than 50 x 20 m. The mineral assemblage is quartz, plagioclase, mica, biotite, garnet, staurolite and kyanite. Accessories are tourmaline, sphene and ilmenite. Dependent on the grade of retrograde metamorphism, intense crystallisation of chlorite can be observed. Staurolites is rimmed and pseudomorphed by sericite aggregates. Plagioclase is also altered and shows deformation twins. Microstructures show asymmetric pressure shadows around the garnets and sub-grain boundary recrystallisation of quartz.

In the southern branch of the study area occur WSW striking layers of biotite-rich paragneisses. Modal mineralogy consists of quartz, plagioclase mica and biotite. Accessories are garnet, staurolite, kyanite and microcline. Chlorite and epidote occur in small scale shear zones. Snowball structures in garnet are typical of syn-deformational growth. Nests and layers of green amphiboles occur in the periphery to amphibolites. Monomineralic quartz layers up to 5 cm thickness are common. Quartz microstructures show recrystallisation by subgrain boundary rotation (SGR) and grain boundary migration (GBM). Quartz ribbons indicate a static recrystallisation during the retrograde phase.

The variety of metabasites ranges from amphibolitized eclogite, garnet-amphibolite and amphibolite to biotite-hornblende-gneiss with folded layers of calcsilicate gneiss. The unit shows in mean a smooth, zonal, anastomosing, sometimes gradational foliation. The amphibolitized eclogite can be observed in small, often altered lenses elongated several meters. Clinopyroxene and plagioclase appear exclusively in coarse-grained symplectites. Primary clinopyroxene has not been found. Garnet displays sieve-like internal structures and is often replaced by mica and feldspar.

146 The amphibolites and hornblende gneisses are mainly composed of green amphibole and
147 plagioclase. Green amphibole has fringes by actinolite and chlorite. Garnet up to 2 cm in diameter
148 overgrows the foliated main fabric, indicating a crystallisation at a late stage of microstructure
149 formation. Plagioclase often displays saussuritisation. Epidote is characterised by core-rim-
150 structures.Quartz with subgrain boundary rotation recrystallisation forms layers parallel to the
151 foliation.
152
153 The calcsilicate gneiss forms folded lenses and layers within amphibolite and plagioclase-
154 hornblende-gneisses. The SW-NE striking layers follow the main foliation and are associated to the
155 northern rim of metabasite zone (Purtscheller, 1978). The protoliths are syn-sedimentary
156 carbonate and marl layers. Often a fluent transition to surrounding lithology can be observed. This
157 often goes ahead with increasing occurrence of ore minerals and gradational interbedding. Modal
158 mineralogy is made of plagioclase, quartz, epidote, chlorite, garnet, wollastonite, Ca-amphibole
159 and mica. Garnet is often pseudomorphed to batches composed of plagioclase, quartz, epidote
160 and chlorite.
161
162
163 **3. Structures and tectonic setting**
164 The Oetztal-Stubai basement can be divided into two tectonic domains (Purtscheller, 1978;
165 Egglseder and Fügenschuh, 2013): (1) Pre-Mesozoic large amplitude open folds in the northern
166 part and (2) the large-scale Schlingen-structures in the southeastern part around Vent. In the
167 studied area, these large-scale fold structures (F_3) deform a pre-Mesozoic steeply N- and S-
168 dipping main foliation S_2. Sub-horizontal to slightly ESE-WNW plunging non-cylindric parasitic folds
169 F_3 are minor structures of this large-scale folds. The geometrical interpretation of the S_2 main
170 foliation planes in the Alpeiner Valley reveals a 5 km scale gentle cylindric fold (Egglseder and
171 Fügenschuh, 2013) with a fold axis slightly plunging to NE. The π-pole at 024/27 was calculated by
172 an Bingham axial distribution (cylindrical best fit) with OSX Stereonet (Cardozo and Allmendinger,
173 2013). The additionally calculated conical best fit axis coincides with the axis from cylindrical best
174 fit. The regional major fold pattern is South-vergent with a WNW-ENE trending fold axis (Egglseder

and Fügenschuh, 2013). Same study revealed a mixed Type 2/3 fold interference pattern (Ramsay and Huber, 1987) for pre-Alpine two-stage folding (F_2-F_3). Measured axes of monocline second order folds result in a mean vector of L 038/39. The calculated π-pole coincides with the 95% confidence interval of the measured second order fold axes (Fig. S1). The second order folds (F_3) are outstandingly visible in the units of the Wechselserie, where they are composed of calcsilicates or monomineralic quartz layers.

At least, six deformation stages (e.g., Purtscheller, 1978; Egglseder and Fügenschuh, 2013) can be observed in the study area: Large amplitude isoclinal folding F_2 was originated parallel to the stretching direction during intense shearing D_1-D_2. This deformation is expressed in small scales by isoclinally folded quartz-veins and calcsilicate layers. D_2 is associated to the formation of the main foliation (S_2 and fold axes F_2) and isoclinal folds F_2 of quartz layers. The deformation stages D_1-D_2 and D_3 belong to the pre-Alpine events, because the axial traces and foliations are not observed in the Brenner Mesozoic (Egglseder and Fügenschuh, 2013). Also mineral cooling ages (Thöni, 1999) imply no Alpine (Cretaceous) metamorphic event with ductile deformation in the northern parts of the Oetztal-Stubai Complex. The subsequent Alpine deformations display an increasing brittle component (Egglseder and Fügenschuh, 2013): W to NW directed thrusts are related to a Cretaceous thrusting. This stage is not observed in the study area. A subsequent top-to-SE directed shearing, appears to be related to a late Cretaceous extension. This stage is observed in the two-mica porphyroblastic gneiss in the south-eastern part of the study area. Then followed small scale NNW to SSE vergent brittle thrusts, related to thrusting of Austroalpine units upon Penninic units. The final brittle stage are NE- and NW-trending strike-slip faults, related to Miocene to Neogene lateral extrusion and exhumation of Tauern Window (Ratschbacher et al., 1991; Egger, 1997). One of these NE-SW striking faults can be observed in the western part of the Rinnengrube. Also sub-vertical NE-SW trending Mohr-fracture systems belong to this stage (Fig. S1).

4. Analytical methods

204 **4.1. SEM-based automated mineralogy (MLA)**

205 Automated mineralogical methods (e.g. Fandrich et al., 2007), based on a scanning electron
206 microscope SEM Quanta 650-FEG-MLA by FEI Company, equipped with Bruker Dual X-Flash
207 energy dispersive spectrometers for EDX analyses were applied to complete thin sections of
208 garnet micaschists. Electron beam conditions were set at 25 kV acceleration voltage at spotsize
209 5.0, which corresponds to beam current of 10 nA. A software package for mineral liberation
210 analysis (MLA version 2.9.0.7 by FEI Company) was used for the automated steerage of the
211 electron beam for EDX identification of mineral grains and collection of numerous EDX spectra.
212 The following measurement routines were applied:
213
214 1) The SPL (Selected Phase Lineup) routine combines a backscattered electron (BSE) grey colour
215 value trigger and single spot EDX-ray spectral analysis. This enables the detection of rare phases
216 as monazite and xenotime and their surrounding minerals. One receives a catalogue of all
217 monazite and xenotime intermineral relationships. This was used to select monazite grains for
218 detailed EMP analysis.
219
220 2) The GXMAP routine produces a narrow grid of ~ 1600 single EDX-ray spectra per mm^2. Garnet
221 and biotite were chosen as the target phases. For the classification of mineral phases and
222 compositions in SPL and GXMAP measurements, a list of identified reference EDX-ray spectra
223 was established by collecting spectra from matrix phases and from defined parts of several garnet
224 porphyroblasts (core - mid - rim). Garnet reference spectra are characterized by EDX-ray single
225 spot elemental analyses which revealed strong variations of Fe, Mg, Mn and Ca in the
226 porphyroblasts. In a next step, the reference spectra were labelled in a generic way with the
227 corresponding garnet Fe-Mg-Mn-Ca compositions. When the labelled spectra are arranged in a
228 color scale, they correspond to semi-quantitative garnet zoning maps (Fig. 3a). The GXMAP
229 measurements were classified against the reference EDX-ray spectra list with a high degree of
230 probability of match. The GXMAP measurements allowed to select a few typical garnets out of
231 dozens of porphyroblasts for quantitative WDS analysis with electron microprobe (EMP).
232

3.2. Electron microprobe (EMP) and monazite dating

The mineral-chemical analyses from metabasite and metapelite samples and were performed with a JEOL JXA-8900-RL instrument at beam conditions of 15 kV, 20 nA, 2 µm, and with the corresponding ZAF correction procedures. The ~900 analytical points on garnet, mica, feldspar, amphibole, clinopyroxene and epidote from the metapelite and metabasite samples enclose detailed garnet zonation traverses.

EMP-Th-U-Pb dating is based on the observation that common Pb in monazite (LREE, Th)PO_4 is negligible when compared to radiogenic Pb resulting from the decay of Th and U (Montel et al., 1996). Electron microprobe analysis of the bulk Th, U and Pb concentrations in monazite, at a constant $^{238}U/^{235}U$, allows for the calculation of a chemical model age (CHIME) with a considerable error (Jercinovic et al., 2008; Montel et al., 1996; Pyle et al., 2005; Spear et al., 2009; Suzuki and Kato, 2008). The Mα1 lines of Th and Pb and the Mβ1 lines for U of a PETH crystal were selected for monazite analysis. Analytical errors of 2σ at 20 kV acceleration voltage, 100 nA beam current, 5 µm beam diameter and counting times of 320 s (Pb), 80 s (U) and 40 s (Th) on peak have been considered for the calculations of ages. For Pb the error ranges typically from 0.016-0.024 wt. % for the given dwell time, based on measurement on a reference monazite (Madmon). Orthophosphates of the Smithsonian Institution were used as standards for REE analysis (Jarosewich and Boatner, 1991). Calibration of PbO was carried out on a vanadinite standard. The U was calibrated on a glass standard with 5 wt% UO_2. A reference monazite labelled as Madmon, with special ThO_2*-PbO characteristics (Schulz and Schüssler, 2013) was used for calibration and offline re-calibration of ThO_2 as well as for the control of data. Interference of YLγ on the PbMα line was corrected by linear extrapolation as proposed by Montel et al. (1996). An interference of ThMγ on UMβ was also corrected. The number of single analyses varies with the grain size of the monazites, e.g. 1-2 analyses in grains of <40 µm and up to 10 analyses in grains of 100 µm in diameter. Monazite chemical ages were first calculated using the methods of Montel et al. (1996). The error resulting from counting statistics was typically on the order of ±20 to ±40 Ma (1σ) for Palaeozoic ages. Weighted average ages for monazite populations calculated using Isoplot 3.0 (Ludwig, 2001) are interpreted as the time of closure for the Th-U-Pb system of monazite during

growth or recrystallisation in the course of metamorphism. Ages were further determined using the ThO_2*–PbO isochrone method (CHIME) of Suzuki et al. (1994) and Montel et al. (1996) where ThO_2* is the sum of the measured ThO_2 plus ThO_2 equivalent to the measured UO_2. This is based on the slope of a regression line in ThO_2* vs PbO coordinates forced through zero. In all analysed samples, the model ages obtained by the two different methods coincide within the error.

5. Mineral chemistry and geothermobarometry

5.1 Metapelites

The garnet- and staurolite bearing micaschists (RZ33 and RZ42) show an overall mineral assemblage of garnet, kyanite, staurolite, biotite, muscovite, plagioclase and quartz. Sample RZ42 is an aluminous gneiss and contains all three Al_2SiO_5-phases. The aluminosilicates are not in invariant equilibrium, as andalusite statically overgrows the foliated fabric with kyanite and sillimanite, as it also has been described by Purtscheller (1978). Garnet is variable in shape and size. Crystals range from small (1 mm) isometric to several mm large subhedral to euhedral grains (Fig. 3a). Inclusions of ilmenite, titanite, mica, quartz and plagioclase can line up to an internal foliation S_1i. Asymmetric pressure shadows by quartz and mica imply a high fraction of simple shear during generation of the external foliation S_2. Garnet zonations show a core-to rim trend with decreasing spessartine (Sps 15 - 1 mole%, calculated from mole fraction*100) and grossular (Grs 20 - 10 mole%), and increasing pyrope (Prp 5 - 20 mole%) (Fig. 3a - d). Some garnets display retrogressive spessartine rich overgrowths. Such rim zones are characterised by strong decrease of the pyrope component (Fig. 3b, c). Staurolite, sometimes twinned and up to 2 mm in size, can be observed. Staurolite within the matrix is not zoned and chemically homogeneous with $Fe_{tot}/(Fe_{tot} + Mg)$ ratio of 0.87 to 0.91 and 11.7 to 13.4 wt% FeO. Staurolite inclusions in garnet are richer in Fe exhibiting a $Fe_{tot}/(Fe_{tot} + Mg)$ ratio of 0.65 and FeO_{tot} of 26.5 wt%. Biotite defines together with muscovite the main foliation. Single biotites are not zoned. Dependent on the sample, they display only little differences in composition with an overall range of *X*Mg between 0.42 and 0.47 (sample RZ42), and *X*Mg between 0.38 and 0.55 (sample RZ33). Among the microstructures, three different positions of biotite can be distinguished (Tropper and Recheis, 2003): (1) Biotites aligned

291 along the main foliation, (2) Biotite as inclusions in garnet with evolving Ti-contents from 0.08 to
292 0.10 (p.f.u.), and (3) Biotite in pressure shadows of garnets formed by the breakdown reaction of
293 garnet = biotite + sillimanite + quartz. These biotites have highest Ti-contents (0.10 - 0.12). Matrix
294 plagioclase shows a trend with An-rich (An_{30}) cores to albite-rich rims (An_{5-10}). Plagioclase grains
295 within garnet (An_{25-30}) and in the pressure shadows (An_{10-20}) show lower An-contents. Aggregates
296 with sericite are formed by breakdown reaction of staurolite and plagioclase during retrogression.
297
298 The garnet zonations in the metapelite samples represent segments of a common mineral-
299 chemical trend, as can be demonstrated in the *X*Mg-*X*Ca coordinates (Fig. 3d). A crystallization of
300 the garnet first at increasing temperature and pressure, then during decompression at amphibolite
301 facies conditions, followed by decompression-cooling can be semiquantitatively derived from the
302 zonations in the *X*Mg-*X*Ca coordinates (Spear, 1993). Cores of garnet and matrix plagioclase as
303 well as relic mica and inclusion minerals in garnet should document the early stage of
304 metamorphism. Late stage metamorphic evolution is preserved in rims of matrix plagioclase and
305 garnet and plagioclase and large biotite in pressure shadows and microlithons. Thus,
306 representative and distinct single analysis of garnet, plagioclase and biotite were chosen in each
307 sample and labeled in the zonation diagrams (Fig. 3a-d, Table 1). Each single garnet zonation
308 trend represents a segment in the overall P-T evolution. Accordingly, the garnet-biotite Fe-Mg
309 exchange geothermometer and the garnet-plagioclase Ca-net-transfer geobarometers (Hodges
310 and Spear, 1982) were chosen. The latter are established as linearised garnet-alumosilicate-
311 plagioclase-quartz (GASP) geobarometers. The datasets are based on internally consistent
312 thermodynamic data given by Hodges and Spear (1982) and Spear and Kohn (1999). P-T were
313 calculated by the program GTB OSX (Spear and Kohn, 1999). Alternatively, temperatures were
314 estimated by the garnet-biotite geothermometers by Battacharya et al. (1992), and Holdaway
315 (2001). Pressures were also calculated with the garnet-aluminosilicate-plagioclase-quartz (GASP)
316 and the garnet-biotite-muscovite-plagioclase (GBMP) geobarometers, enclosing the internally
317 consistent thermodynamic mineral data set (Holland and Powell, 1998), with the activity models for
318 garnet and plagioclase taken from Powell and Holland (1993) and Ganguly et al. (1996), and the
319 empirical re-calibration of the GBMP barometer by Wu (2015).

In detail and dependent on Mn bulk rock compositions, garnet cores started to crystallise at ~ 460 - 500 °C/7 - 8 kbar (Fig. 4a). Then maximal pressures at around 12 kbar were achieved at 680 °C. This was followed by a decompression to 6 kbar, accompanied by only slight cooling to 660 °C. The Mg-poor and Mn-enriched marginal zones of some garnets signal a cooling and decompression toward 590 °C/4 - 6 kbar (Fig. 4a). Geothermobarometric estimates include a minimum error of ± 35°C and ± 1 kbar (Spear and Kohn, 1999). Thus, resulting errors of thermobarometric calculations are much higher than quantitative systematic error in thermodynamic data and microprobe analysis. If these facts are considered, the P-T path's shape and/or relative $\Delta P/\Delta T$ trends will be obtained. When applied to garnet cores and rims in the samples RZ33 and RZ42, the single P-T segments line up to a clockwise prograde-retrograde P-T path (Fig. 4a).

5.2 Metabasites

Two metabasite samples were selected for mineral chemistry analyses and related geothermobarometry. Sample RZ 24 is an amphibolitized eclogite (Purtscheller, 1978). Garnets are up to 3 mm in diameter in a matrix composed of fine-grained symplectites, green amphiboles, plagioclase, epidote and quartz. Titanite and ilmenite appear as the Ti-bearing phases. From cores to rims the garnets are zoned with decreasing spessartine (Sps 12 to 1 mole%, calculated from mole fraction*100), strongly increasing pyrope (Prp 5 - 25 mole%) at quite constant high grossular (Grs 22 - 25 mole%). This pyrope zonation trend indicates crystallization at increasing temperature. The Mg- and Ca-rich garnet rim compositions are typical of eclogites without coesite. In combination with the symplectites this indicates a former eclogitic stage for the Alpeiner amphibolite unit. Many inclusions of epidote towards the garnet rim are typical. Plagioclases are slightly zoned, sometimes with oligoclase cores, but mostly with albitic compositions at An < 10. Plagioclase is also albitic in the symplectites with secondary clinopyroxene with Jd < 10. Ca-amphiboles in the metabasites display considerable zonations and compositional variations which can be described best in ^{IV}Al vs. ^{VI}Al coordinates (Fig. 3e) and also in the Si vs *X*Mg nomenclature diagram (Fig. 3f) after Leake et al. (1997). Amphibole cores in sample RZ24 have high ^{VI}Al (~ 3.8

p.f.u.) of ferro-tschermakite and rims with lower ^{VI}Al (1.0) at similar ^{IV}Al (1.6). In sample RZ37 one observes amphibole cores with Mg-hornblende compositions at ^{VI}Al of 1.5 and ^{IV}Al of 1.2 - 1.6 (p.f.u.). In this sample, amphibole rims and also a second generation of porphyroblasts are actinolites with ^{VI}Al and ^{IV}Al below 0.4 (Fig. 3e,f).

The garnet-clinopyroxene Fe-Mg geothermometer cannot be used for sample RZ24, as the only observed clinopyroxene in the symplectites has low Na (Jd < 10) and no Na-rich clinopyroxene corresponding to the eclogitic stage remained preserved. The dependence of Si and ^{IV}Al on temperature and ^{VI}Al on pressure in Ca-amphiboles in assemblages with plagioclase, epidote, quartz, ilmenite and/or titanite can be used for P-T estimates. The amphibole-bearing assemblages in samples RZ24 and RZ match the requirements for the application of the geothermobarometer of Zenk and Schulz (2004) which involves experimental data listed by Gerya et al. (1997). Accordingly, the zoned ferro-tschermakitic to tschermakitic amphiboles in sample RZ24 crystallized during a nearly isothermal decompression from 11 to 6 kbar at 680 - 600 °C (Fig. 4b). The Mg-hornblende and actinolites in sample RZ37 crystallized at mainly decreasing temperatures from 600 to 400 °C/4 - 2 kbar (Fig. 4b). The P-T estimates from the metabasites contribute with retrograde P-T segments to the overall clockwise P-T path of the Alpeiner series.

6. Monazite ages and mineral chemistry

In the garnet micaschists the monazite appears in different grain sizes and microstructural associations (Fig. 6). Grains with an elongated shape and an average length of 200 µm and width of 50-150 µm allowed for up to 15 single spot analysis. The grains are parallel to S_2 foliation. Large monazite with slightly embayed grain boundaries show partly darker zones in the backscattered electron (BSE) images (Fig. 5a, b). The single ages in these large grains vary from Carboniferous to Permian (320 - 250 Ma), with Permian weighted average ages. No systematic variation of the ages with the darker core and the lighter rim zones with higher ThO_2 contents are observed. A strongly embayed large monazite gives a Triassic weighted average age due to numerous Jurassic to Cretaceous single ages apart from the Permian ages (Fig. 5c). In samples RZ31 and RZ29, one

observes Permian monazite with the double corona structure by apatite and allanite. The apatite-allanite corona structures around Permian monazite (Fig. 5d-f) are interpreted as an indicator for monazite decomposition. Monazite is progressively replaced in stages by apatite accompanied by formation of allanite surrounding apatite. The initial stage of corona formation is characterized by single tiny apatite grains which have crystallized between an allanite corona and monazite (Fig. 5d). The next stage is a continuous corona of apatite around monazite, which itself is surrounded by a mantle of allanite. The allanite mantle is composed of crystals with radial orientation (Fig. 5d-f). This can be explained by pseudomorphic partial replacement of the original monazite by apatite and allanite via a fluid-mediated coupled dissolution-precipitation process (Harlov et al., 2011; Budzyń et al., 2011). At the present stage of knowledge, such monazite corona structures are generated during decreasing pressure and temperature (Broska and Siman, 1998; Budzyń et al., 2011; Finger et al., 1998; Krenn and Finger, 2007), and retrogression (Upadhyay and Pruseth, 2012). When the weighted average ages of monazites in the corona structures are compared, a systematic shift from Permian ages in well preserved monazite cores (Fig. 5d) toward Triassic and Jurassic ages in tiny thin monazite relics in the coronas (Fig. 5f) can be stated.

Another microstructural feature are clusters composed of numerous small monazite grains with diameters of mostly < 10 µm (Fig. 5g-h). These small monazite grains are surrounded by allanite. The cluster monazite in association with allanite, plagioclase, mica display mostly Permian to Triassic ages. This arrangement of cluster monazite are distinct from the satellite monazite structure as it was described by Finger et al. (2016). The satellite monazite microstructure are small grains arranged around a larger central grain and is considered as the new crystallization of monazite in a former apatite-allanite double corona structure when monazite stability conditions are attained by re-increasing temperature after a retrogression. In contrast, the monazite clusters apparently pseudomorph large mica. Each of the small monazite grains is embedded and surrounded by allanite. However, at the present limited stage of knowledge about this structure, the Permo-Triassic monazites in the clusters represent at least a period of intense re-crystallization.

407 The monazites in the three studied samples display a diverse mineral chemistry. In the age vs
408 Y_2O_3 plot, monazite in sample RZ29 are mostly high in Y_2O_3 (up to 3 wt%), whereas in sample
409 RZ42 they are mostly low in Y_2O_3 (0.2 - 1.5 wt%). In sample RZ31 the whole compositional range
410 of Y_2O_3 contents occur (Fig. 6a). Overall, the contents of LREE, and also ThO_2 (1.5-6 wt%) and
411 UO_2 (0.1-1.6 wt%) are within the range of metamorphic monazites (Spear and Pyle, 2002, Wing et
412 al., 2003). In the age vs UO_2, *X*HREE+Y vs *X*LREE and also in the *X*$GdPO_4$ vs *X*YPO_4 plots,
413 overlapping trends are observed in the three samples (Fig. 6b-d). The *X*YPO_4 slightly exceed the
414 limit of the garnet zone or garnet isograd as given by Pyle et al. (2001), but do not reach the limit
415 between the sillimanite zone and migmatism (Fig. 6d). The *X*Hutt is negligeable and the *X*Cher in
416 most monazites ranges from 0.05 to 0.15 (not shown). The dominant cheralite exchange (Th or U
417 + Ca = 2 REE) is typical for systems with elevated Ca (Spear and Pyle, 2002). Monazites in
418 sample RZ42 strictly follow the cheralite substitution trend in Th+U vs Ca coordinates (Fig. 6e). In
419 contrast, the monazites in samples RZ31 and especially sample RZ29 with many Triassic ages
420 deviate from the pure cheralite substitution trend and display almost constant Ca at increasing
421 Th+U (Fig.6e).
422
423 In the histogram view, the distribution of single spot ages display a prominent maximum in the
424 Permian (280 - 270 Ma) and a second and considerably lower maximum in Triassic times at 230 -
425 220 Ma (Fig. 6f). Only a few Carboniferous ages appear in the histogram view. Cretaceous ages
426 are also rare. As expressed in the histogram, in the single large grains and the cluster weighted
427 average mean ages (Fig. 5), several isochrons can be defined in the single samples. However, all
428 these isochrones are mainly established by sorting of the data and are characterised by low values
429 of R^2 and weak MSWD. Carboniferous isochrones at 304 ± 26 Ma (sample RZ42) and 321 ± 33 Ma
430 (sample RZ31) are poorly defined and underlined by only a few data (Fig. 7a, b). The Permian age
431 isochrones at 272 ± 15 Ma (RZ42) and 269 ± 13 Ma (RZ31) enclose a considerable number of
432 single ages. For sample RZ29 the Permian isochrone at 252 ± 31 Ma is poorly defined with a few
433 data and most monazite ages fall into the Triassic (202 ± 34 Ma, Fig. 7c). In the other samples,
434 one can also calculateTriassic isochrones at 215 ± 59 Ma and 209 ± 17 Ma, which sometimes can
435 be defined by monazites with lower ThO_2* (Fig. 7a, b)

436

437 **7. Discussion and Conclusions**

438 The combination of the thermobarometric results from garnet metapelites and metabasites in the
439 Alpeiner Valley points to a clockwise P-T path which evolved mainly in the high-pressure
440 amphibolite-facies. The prograde P-T path started in the kyanite stability field. Maximal pressures
441 and temperatures range around 12 kbar and 680 °C. Then the P-T path passed the sillimanite field
442 at decreasing pressure. Zoned green amphiboles recorded conditions from 4 - 5 kbar/600 °C to 2
443 kbar/400 °C, indicating a retrograde P-T path which entered the andalusite stability field (Fig. 8a).
444 This matches the observation of the three alumosilicates in sample RZ42, where andalusite
445 overgrows the fabric at a late stage of the evolution. By a comparison to P-T data and paths from
446 garnet metapelites in adjacent parts of the Oetztal-Stubai Complex (e.g., Schulz, 1994; Tropper
447 and Recheis, 2001; Rode et al., 2012), it appears likely that the amphibolite-facies metamorphism
448 in the Alpeiner Valley matches the Variscan (Carboniferous) event described from the Sellrain,
449 Umhausen and Sölden areas (Fig. 8a). It was not possible to constrain eclogite facies P-T
450 conditions in the Alpeiner Valley metabasites, as it has been described from the Central
451 Metabasite Zone (CMBZ) in the Oetztal (Miller and Thöni, 1995; Rode et al., 2012). Omphacite
452 with high jadeite contents was not preserved in the Alpeiner Valley metabasites. However, the
453 pervasive occurrence of symplectites with low jadeite bearing clinopyroxene demonstrates that the
454 metabasites should have experienced somewhat higher pressures as were actually recorded by
455 the green amphiboles.

456

457 It appears tempting to relate the pressure-dominated amphibolite-facies metamorphism in the
458 Alpeiner Valley to the pervasive crystallisation of Permian to Triassic monazites. However, the
459 similarity of the P-T path from the Alpeiner Valley to the Carboniferous P-T paths from the Oetztal
460 (Fig. 8a) counts against such an interpretation. Also the monazite phase stability limits should be
461 considered in this discussion. Studies in amphibolite-facies metapelites have identified a major
462 pulse of monazite growth, which could be linked to the breakdown of garnet at decreasing
463 pressure (Pyle and Spear, 1999; Pyle et al., 2001; Spear, 2010). In fact, the P-T record in the
464 metapelite garnet ceased during decompression. This could explain the wide variety of Y in

465 monazite which crystallized subsequent to the garnet and which could have incorporated the Y
466 from decomposed garnet. According to Janots et al. (2007), Spear (2010), Spear and Pyle (2010)
467 and Goswami-Banerjee and Robyr (2015), monazite is stable under amphibolite-facies conditions.
468 The temperature-dependent univariant allanite-monazite equilibrium with the monazite stability limit
469 is qualitatively shifted toward lower temperature with decreasing Ca and increasing Al in the bulk
470 rock (Fig. 8a). Within this frame, monazite should have crystallized when the actual P-T path
471 passed the allanite-monazite stability limit at decreasing pressure (Fig. 8a). Considering *X*Ca and
472 *X*An in garnet and plagioclase, and the occurrence of the metapelite layers within a rock suite
473 dominated by metabasites, the Alpeiner Valley garnet micaschists should have considerably higher
474 bulk rock Ca when compared to the aluminous micaschist samples at Umhausen, Sölden and
475 Sellrain as reported by Rode et al. (2012). This implicates that most of the Alpeiner Valley
476 monazite should have crystallized at comparably lower pressures and at a late stage, when the
477 decompression P-T path passed from the sillimanite to the andalusite stability field (Fig. 8a). If this
478 is accepted, the P-T evolution within the kyanite and sillimanite stability fields should be also
479 Carboniferous in the Alpeiner Valley, as was similarily reported from the adjacent Sellrain,
480 Umhausen and Sölden micaschists (Rode et al., 2012). Monazite isochrones at 324 ± 27 Ma
481 (sample RZ31) and 304 ± 26 Ma (sample RZ42) support this interpretation. These poorly defined
482 isochrones (Fig. 7a, b) are assembled by disperse single monazite analyses within larger grains.
483
484 The bulk of monazite analyses is related to isochrones at 272 ± 15 Ma and 260 ± 12 Ma, partly
485 with a broad cluster of the data around the regression, and a maximum in the histogram at ~270
486 Ma (Fig. 7b, c, 8b). One sample (RZ29) displays a Triassic isochrone (Fig. 7a), however, in the
487 histogram view a sub-maximum of ages appears at ~220 Ma (Figs 5f, 8b). When compared to the
488 monazite age data from the Sellrain, Umhausen and Sölden regions (Rode et al., 2012), with their
489 unimodal age distributions around 317 ± 5 Ma, the mostly Permian Alpeiner Valley monazites
490 apparently indicate a distinct thermal event in the histogram distribution (Fig. 8b). However, in the
491 Alpeiner Valley on one hand large Permian monazite grains were consumed during retrogression
492 in the double corona structures. On the other hand. the monazite cluster structures support a new
493 crystallization of monazite in domains of allanite.Their age pattern also differs from observations

494 from the Austroalpine basement to the south of the Tauern Window, where bimodal Carboniferous
495 and Permian monazite age distributions occur (Krenn et al., 2012). The monazite age pattern of
496 Alpeiner Valley also differs from the Eclogite Unit of the Saualpe to the E of the Tauern Window,
497 where Cretaceous monazite is abundant apart a Permian population (Schulz, 2016). Permian
498 metamorphic and magmatic ages have yet been mainly reported from Austroalpine basement
499 domains where numerous intrusions of Permian pegmatites occurred (Schuster et al., 2001;
500 Schuster and Stüwe, 2008, and references therein). Evidently, the fluid activity associated to these
501 intrusions enhanced the monazite crystallisation in metapelites, when low pressure and low bulk
502 Ca compositions are given.
503
504 There are yet no own observations or reports of pegmatites and Permian pegmatites respectively
505 from the Alpeiner Valley and the OSC nearby. As a consequence, the P-T path and the monazite
506 ages from the Alpeiner Valley may be considered as a link between the Austroalpine domains with
507 exclusively Carboniferous high-pressure amphibolite to eclogite facies metamorphism, and the
508 domains with the Permian event evidently manifested by the pegmatites. The observations from
509 the Alpeiner Valley also indicate that a distinct Permian to Triassic thermal event appeared after a
510 precedent Carboniferous collisional crustal thickening, as proven by clockwise P-T paths.
511
512 The nature and geodynamic significance of a Permian to Triassic event in the Austroalpine and
513 also Southalpine basement units has been increasingly discussed with the emerging new age data
514 and the re-interpretation of existing data (Schuster et al., 2001). According to Schuster and Stüwe
515 (2008), the Permian event can be related to (1) intrusion of Permian gabbros into the middle and
516 lower crust, (2) granite and pegmatite intrusions at mid-crustal levels, (3) quartz-andalusite veins
517 and (4) Permian volcanics. These Permian magmatic features are possible in an extensional
518 tectonic cycle as outlined by Schuster and Stüwe (2008). The P-T data from the Alpeiner
519 metamorphic rocks provide no detailed resolution of the Permian to Triassic event in terms of a re-
520 heating and then further cooling path at low pressures. However, the monazite age data at least
521 documents a prolonged, decelerated, and possibly more complex post- Permo-Triassic history
522 subsequent to the Carboniferous amphibolite facies stage. By comparison to P-T-t data from the

adjacent Oetztal, it is also evident that monazite age data not necessarily refers to the garnet crystallization during the main metamorphic event in the basement, but can give witness to a subsequent geodynamic evolution at lower pressures.

Acknowledgements

The electron-microprobe monazite dating and silicate analyses required long-term analytical sessions with technical assistance through D. Heger, Institut für Werkstoffwissenschaft der TU Freiberg. Support at the SEM studies in the Laboratory of Geometallurgy at Freiberg was provided by K. Bachmann and S. Haser. R. Zimmermann thanks the team of Franz-Senn Hütte for hospitality during field work in 2013.

References

Bhattacharya, A., Mohanty, L., Maji, A., Sen, S.K. and Raith, M., 1992. Non-ideal mixing in the phlogopite-annite binary: constraints from experimental data on Fe-Mg partitioning and a reformulation of the garnet-biotite geothermometer. Contributions to Mineralogy and Petrology, 111, 87–93.

Broska, I., and Siman, P., 1998. The breakdown of monazite in the West-Capathian Veporic orthogneisses and Tatric granites. Geologica Carpathica, 49, 161–167.

Budzyń, B., Harlov, D.E., Williams, M.L. and Jercinovic, M.J., 2011. Experimental determination of stability relations between monazite, fluorapatite, allanite, and REE-epidote as a function of pressure, temperature, and fluid composition. American Mineralogist, 96, 1547–1567. http://dx.doi.org/10.2138/am.2011.3741

Cardozo, N. and Allmendinger, R.W., 2013. Spherical Projections with OSXStereonet. Computers and Geosciences, 51, 193–205. http://dx.doi.org/10.1016/j.cageo.2012.07.021

552

553 Egger, H., 1997. Das sinistrale Innsbruck-Salzburg-Amstetten-Blattverschiebungssystem: Ein
554 weiterer Beleg für die miozäne laterale Extrusion der Ostalpen. Jahrbuch der geologischen
555 Bundesanstalt, 140/1, 47–50.

556

557 Egglseder, M. and Fügenschuh, B., 2013. Pre-Alpine fold interference pattern in the northeastern
558 Oetztal-Stubai Complex (Tyrol, Austria). Austrian Journal of Earth Sciences, 106/2, 63–74.

559

560 Fandrich, R., Gu, Y., Burrows, D. and Moeller, K., 2007. Modern SEM-based mineral liberation
561 analysis. International Journal of Mineral Processing, 84, 310–320.
562 http://dx.doi.org/10.1016/j.minpro.2006.07.018

563

564 Finger, F., Broska, I., Roberts, M. and Schermaier, A., 1998. Replacement of primary monazite by
565 allanite-epidote coronas in an amphibolite-facies granite gneiss from the eastern Alps. American
566 Mineralogist, 83, 248–258. http://dx.doi.org/10.2138/am-1998-3-408

567

568 Finger, F., Krenn, E., Schulz, B., Harlov, D.E. and Schiller, D., 2016. Satellite monazites in
569 polymetamorphic basement rocks of the Alps: their origin and petrological significance. American
570 Mineralogist, 101, 1094–1103. http://dx.doi.org/10.2138/am-2016-5477

571

572 Frey, M., Desmons, J. and Neubauer, F., 1999. The new metamorphic map of the Alps. Swiss
573 Bulletin of Mineralogy and Petrology, 79, 1–4.

574

575 Frisch, W., Dunkl, I. and Kuhlemann, J., 2000. Post-collisional orogen-parallel large-scale
576 extension in the Eastern Alps. Tectonophysics, 327, 239–265. http://dx.doi.org/10.1016/S0040-
577 1951(00)00204-3

578

579 Ganguly, J., Cheng, W. and Tirone, M., 1996. Thermodynamics of aluminosilicate garnet solid
580 solution: new experimental data, an optimized model, and thermometric applications. Contributions

581 to Mineralogy and Petrology, 126, 137–151. http://dx.doi.org/10.1007/s004100050240
582
583 Gerya, T., Perchuk, L., Triboulet, C., Audren, C. and Sezko, A.,1997. Petrology of the Tumanshet
584 Zonal Metamorphic Complex, Eastern Sayan. Petrology, 5/6, 503–533.
585
586 Goswami-Banerjee, G. and Robyr, M., 2015. Pressure and temperature conditions for
587 crystallization of metamorphic allanite and monazite in metapelites: a case study from Miyar Valley
588 (high Himalayan Crystalline of Zanskar, NW India). Journal of Metamorphic Geology, 33, 535–556.
589 http://dx.doi.org/10.1111/jmg.12133
590
591 Hammer, W., 1929. Geologische Spezialkarte der Republik Österreich - Blatt Ötztal (5146).
592 Geologische Bundesanstalt in Wien
593
594 Harlov, D.E., Wirth, R. and Hetherington, C.J., 2011. Fluid-mediated partial alteration in monazite:
595 the role of coupled dissolution–reprecipitation in element redistribution and mass transfer.
596 Contributions to Mineralogy and Petrology, 162, 329–348. http://dx.doi.org/10.1007/s00410-010-
597 0599-7.
598
599 Heinrich, W., Andrehs, G. and Franz, G., 1997. Monazite-xenotime miscibility gap thermometry. An
600 empirical calibration. Journal of Metamorphic Geology, 15, 3–17.
601
602 Hodges, K. and Spear, F.S., 1982. Geothermometry, geobarometry and the Al_2SiO_5 triple point at
603 Mt. Moosilauke, New Hampshire. American Mineralogist, 67, 1118–1134.
604
605 Hoinkes, G., Kostner, A. and Thöni, M., 1991. Petrologic constraints for Eoalpine eclogite facies
606 metamorphism in the Austroalpine Ötztal basement. Mineralogy and Petrology, 43, 237–254.
607

608 Hoinkes, G. and Thöni, M., 1993. Evolution of the Ötztal-Stubai, Scarl-Campo and Ulten Basement
609 Units. In: von Raumer, J. F. and Neubauer, F. (eds.), The pre-Mesozoic Geology of the Alps, 485–
610 494, Heidelberg (Springer). pp. 485–494.
611
612 Hoinkes, G., Koller, F. and Rantitsch, G., 1999. Alpine metamorphism of the Eastern Alps.
613 Schweizerische mineralogische und petrographische Mitteilungen, 79/1, 157–181.
614
615 Holdaway, M. J., 2001. Recalibration of the GASP geobarometer in light of recent garnet and
616 plagioclase activity models and versions of the garnet-biotite geothermometer. American
617 Mineralogist, 86, 1117–1129. http://dx.doi.org/10.2138/am-2001-1001
618
619 Holland, T. (1980): The reaction albite = jadeite + quartz determined experimentally in the range
620 600-1200°C. American Mineralogist, 65, 129–134.
621
622 Holland, T.J.B., 1983. The experimental determination of activities in disordered and short-range
623 ordered jadeitic pyroxene. Contributions to Mineralogy and Petrology, 82, 214–220.
624
625 Holland, T.J.B. and Powell, R., 1998. An internally-consistent thermodynamic dataset for phases of
626 petrological interest. Journal of Metamorphic Geology, 16, 309–344.
627
628 Janots, E., Brunet, F., Goffé, B., Poinssot, C., Burchard, M. and Cemic, L., 2007. Thermochemistry
629 of monazite-(La) and dissakisite-(La): implications for monazite and allanite stability in metapelites.
630 Contributions to Mineralogy and Petrology, 154, 1–14. http://dx.doi.org/10.1007/s00410-006-0176-
631 2
632
633 Jarosewich, E. and Boatner, L.A., 1991. Rare-earth element reference samples for electron
634 microprobe analysis. Geostandards Newsletter, 15, 397–399.
635

636 Jercinovic, M.J., Williams, M.L. and Lane, E.D., 2008. In-situ trace element analysis of monazite
637 and other fine-grained accessory minerals by EMPA. Chemical Geology, 254, 197–215.
638 http://dx.doi.org/10.1016/j.chemgeo.2008.05.016
639
640 Klötzli-Chowanetz, E., Klötzli, U. and Koller, F., 1997. Lower Ordovician migmatisation in the Ötztal
641 crystalline basement (Eastern Alps, Austria): linking U-Pb and Pb-Pb dating with zircon
642 morphology. Swiss Bulletin of Mineralogy and Petrology, 77, 315–324.
643
644 Krenn, E. and Finger, F. 2007. Formation of monazite and rhabdophane at the expense of allanite
645 during Alpine low temperature retrogression of metapelitic basement rocks from Crete, Greece:
646 Microprobe data and geochronological implications. Lithos, 95, 130–147.
647 http://dx.doi.org/10.1016/j.lithos.2006.07.007
648
649 Krenn, E., Schulz, B. and Finger, F., 2012. Three generations of monazite in Austroalpine
650 basement rocks to the south of the Tauern Window - evidences for Variscan, Permian and Alpine
651 metamorphism. Swiss Journal of Geosciences, 105, 343–360. http://dx.doi.org/10.1007/s00015-
652 012-0104-6
653
654 Leake, B.E., Woolley, A.R., Arps, C.E., Birch, W.D., Gilbert, M.C., Grice, J.D., Hawthorne, F.C.,
655 Kato, A., Kisch, H.J., Krivovichev, V.G., Linthout, K., Laird, J., Mandarino, J.A., Maresch, W.V.,
656 Nickel, E.H., Rock, N.M.S., Schumacher, J.C., Smith, D.C., Stephenson, N.C., Ungeretti, L. and
657 Whittaker, E.J., 1997. Nomenclature of Amphiboles: Report of the subcommittee in amphiboles of
658 the International Mineralogical Association, commission on new minerals and mineral names. The
659 Canadian Mineralogist, 35, 219–246.
660
661 Ludwig, K., 2001. Users manual for Isoplot/Ex (rev. 2.49): a geochronological toolkit for Microsoft
662 Excel. Berkeley Geochronological Center.
663

664 Marotta, A. M. and Spalla, M.I., 2007. Permian-Triassic high thermal regime in the Alps: Result of
665 late Variscan collapse or continental rifting? Validation by numerical modeling. Tectonics, 26,
666 TC4016. http://dx.doi.org/10.1029/2006TC002047
667
668 Miller, C. and Thöni, M., 1995. Origin of eclogites from the Austroalpine Ötztal basement (Tirol,
669 Austria): geochemistry and Sm-Nd vs. Rb-Sr isotope systematics. Chemical Geology, 122, 199–
670 225.
671
672 Mogessie, A., Purtscheller, F. and Tessadri, R., 1985. Geochemistry of amphibolites from the
673 Ötztal-Stubai Complex (Northern Tyrol, Austria). Chemical Geology, 51, 103–113.
674
675 Mogessi, A. and Purtscheller, F. (1986): Polymetamorphism of the Oetztal-Stubai basement
676 complex based on amphibolite petrology. Jahrbuch der Geologischen Bundesanstalt Wien, 129,
677 69–91.
678
679 Montel, J., Foret, S., Veschambre, M., Nicollet, C. and Provost, A., 1996. A fast, reliable,
680 inexpensive in-situ dating technique: electron microprobe ages on monazite. Chemical Geology,
681 131, 37–53.
682
683 Neubauer, F., Hoinkes, G. and Sassi, F.P., 1999. Pre-Alpine metamorphism of the Eastern Alps.
684 Swiss Bulletin of Mineralogy and Petrology, 9/1, 41–62.
685
686 Powell, R. and Holland, T.J.B., 1993. On the formulation of simple mixing models for complex
687 phases. American Mineralogist, 78, 1174–1180.
688
689 Purtscheller, F., 1978. Ötztaler und Stubaier Alpen, 2nd ed. Sammlung Geologischer Führer Vol.
690 53. Gebrüder Bornträger, Stuttgart, 128 pp.
691

692

693 Pyle, J.M. and Spear, F.S., 1999. Yttrium zoning in garnet: coupling of major and accessory
694 phases during metamorphic reactions. Geological Materials Research 1(6), 1–49.
695
696 Pyle, J., Spear, F., Rudnick, R. and McDonough, W., 2001. Monazite-xenotime-garnet equilibrium
697 in metapelites and a new monazite-garnet thermometer. Journal of Petrology, 42, 2083–2107.
698
699 Pyle J.M., Spear, F.S., Wark, D.A., Daniel, C.G., Storm, L.C., 2005. Contributions to precision and
700 accuracy of chemical ages of monazite. American Mineralogist 90, 547–577.
701 http://dx.doi.org/10.2138/am.2005.1340
702
703 Ramsay, J.G. and Huber, M., 1987. Techniques of Modern Structural Geology, Vol. 2: Folds and
704 Fractures. Academic Press, London, 392 pp.
705
706 Ratschbacher, L., Frisch, W., Linzer, H.G. and Merle, O., 1991. Lateral extrusion in the eastern
707 alps, Part 2: Structural analysis. Tectonics, 10/2, 257–271.
708
709 Rode, S., Rösel, D. and Schulz, B., 2012. Constraints on the Variscan P-T evolution by EMP Th-U-
710 Pb monazite dating in the polymetamorphic Austroalpine Oetztal- Stubai basement (Eastern Alps).
711 Zeitschrift der deutschen Gesellschaft für Geowissenschaften, 163/1, 43–68.
712 http://dx.doi.org/10.1127/1860-1804/2012/0163-0043
713
714 Schmid, S., Fügenschuh, B., Kissling, E. and Schuster, R., 2004. Tectonic map and overall
715 architecture of the Alpine orogen. Eclogae geologicae Helvetiae, 97, 93–117.
716 http://dx.doi.org/10.1007/s00015-004-1113-x
717
718 Schulz, B. 1994. Polyphase Variscan P-T-deformation path from mica schists of the sillimanite
719 zone in the Austroalpine Ötztal-Stubai basement (Eastern Alps). Neues Jahrbuch für Mineralogie
720 Abhandlungen, 168, 47–65.

721

722 Schulz, B. 2014. Early Carboniferous P–T path from the Upper Gneiss Unit of Haut-Allier (French
723 Massif Central) – reconstructed by geothermobarometry and EMP–Th–U–Pb monazite dating.
724 Journal of Geosciences, 59, 327–349. http://dx.doi.org/10.3190/Jgeosci.178

725

726 Schulz, B. 2016. Polymetamorphism in garnet micaschists of the Saualpe Eclogite Unit (Eastern
727 Alps, Austria), resolved by automated SEM methods and EMP-Th-U-Pb monazite dating. Journal
728 of Metamorphic Geology, http://dx.doi.org/10.1111/jmg.12224

729

730 Schulz, B., Brätz, H., Bombach, K. and Krenn, E. 2007. In-situ Th-U dating of monazite by 266 nm
731 laser ablation and ICP-MS with a single collector, and its control by EMP analysis. Zeitschrift für
732 Angewandte Geologie, 35, 377–392.

733

734 Schulz, B. and Schüssler, U. 2013. Electron-microprobe Th-U-Pb monazite dating in Early-
735 Palaeozoic high-grade gneisses as a completion of U-Pb isotopic ages (Wilson Terrane,
736 Antarctica). Lithos, 175-176, 178–192. http://dx.doi.org/10.1016/j.lithos.2013.05.008

737

738 Schuster, R., Scharbert, S., Abart, R. and Frank, W., 2001. Permo-Triassic extension and related
739 HT/LP metamorphism in the Austroalpine - South Alpine realm. Mitteilungen Geologie und
740 Bergbaustudenten Österreich, 44, 111–141.

741

742 Schuster, R. and Stüwe, K., 2008. Permian metamorphic event in the Alps. Geology, 36/8, 603–
743 606. http://www.dx.doi.org/10.1130/G24703A.1

744

745 Söllner, F. (2001): The Winnebach migmatite (Ötz-Stubai crystalline unit) – evidence for a Pan-
746 African metamorphism in an overthrust nappe sequence in the Eastern Alps. Geologische und
747 Paläontologische Mitteilungen der Universität Innsbruck, 25, 199–200.

748

749 Spear, F., 1993. Metamorphic phase equilibria and pressure-temperature-time paths. Mineralogical
750 Society of America Monography Series, No. 1, Mineralogical Society of America. 700 p.
751
752 Spear, F., 2010. Monazite-allanite phase relations in metapelites. Chemical Geology, 279/1–2, 55–
753 62. http://dx.doi.org/10.1016/j.chemgeo.2010.10.004
754
755 Spear, F.S., Pyle, J.M. and Cherniak, D., 2009. Limitations of chemical dating of monazite.
756 Chemical Geology, 266, 218–230. http://dx.doi.org/10.1016/j.chemgeo.2009.06.007
757
758 Spear, F. and Kohn, M.J., 1999. Program GTB GeoThermoBarometry, Version 2.1, Program
759 Manual, http://ees2.geo.rpi.edu/metapetaren/Software/GTB_Prog/GTB.html (accessed on 18.
760 October 2016).
761
762 Spear, F. and Pyle, J., 2002. Apatite, monazite and xenotime in metamorphic rocks. Reviews in
763 Mineralogy and Geochemistry, 48/1, 293–335. http://www.dx.doi.org/10.2138/rmg.2002.48.7
764
765 Spear, F.S. and Pyle, J.M., 2010. Theoretical modeling of monazite growth in a low-Ca metapelite.
766 Chemical Geology, 273, 111–119. http://dx.doi.org/10.1016/j.chemgeo.2010.02.016
767
768 Suzuki, K., Adachi, M. and Kajizuka, I., 1994. Electron microprobe observations of Pb diffusion in
769 metamorphosed dentrital monazites. Earth and Planetary Science Letters, 128, 391–405.
770
771 Suzuki, K. and Kato, T., 2008. CHIME dating of monazite, xenotime, zircon and polycrase:
772 Protocol, pitfalls and chemical criterion of possible discordant age data. Gondwana Research, 14,
773 569–586. http://dx.doi.org/10.1016/j.gr.2008.01.005
774
775 Thöni, M., 1981. Degree and Evolution of the Alpine Metamorphism in the Austroalpine Unit W of
776 Hohe Tauern in the light of K/Ar and Rb/Sr Age Determinations in Micas. Jahrbuch der
777 Geologischen Bundesanstalt Wien, 124, 111–174.

778

779 Thöni, M. (1983): The climax of the early Alpine metamorphism in the Austroalpine thrust sheet.
780 Memorie Science Geologiche Padova, 36, 211–238.

781

782 Thöni, M., 1999. A review of geochronological data from the Eastern Alps. Swiss Bulletin of
783 Mineralogy and Petrology, 79/1, 209–230.

784

785 Thöny, W.F., Tropper, P., Schennach, F., Krenn, E., Finger, F., Kaindl, R., Bernhard, F. and
786 Hoinkes, G., 2008. The metamorphic evolution of migmatites from the Ötztal Complex (Tyrol,
787 Austria) and constraints on the timing of the pre-Variscan high-T event in the Eastern Alps. Swiss
788 Journal of Geosciences, 101 Supplement 1, 111–126. http://www.dx.doi.org/10.1007/s00015-008-
789 1290-0

790

791 Tropper, P. and Hoinkes, G., 1996. Geothermobarometry of Al_2SiO_5-bearing metapelites in the
792 western Austroalpine Ötztal-basement. Mineralogy and Petrology, 58, 145–170.

793

794 Tropper, P. and Recheis, A., 2003. Garnet zoning as a window into the metamorphic evolution of a
795 crystalline complex: the northern and central Austroalpine Ötztal-Complex as a polymorphic
796 example. Mitteilungen der Österreichischen Geologischen Gesellschaft, 94, 27–53.

797

798 Upadhyay, D. and Pruseth, K.L., 2012. Fluid-induced dissolution breakdown of monazite from Tso
799 Morari complex, NW Himalayas: evidence for immobility of trace elements. Contributions to
800 Mineralogy and Petrology, 164, 303–316. http://dx.doi.org/10.1007/s00410-012-0739-3

801

802 Wing, B.A., Ferry, J.M. and Harrison, T.M., 2003. Prograde destruction and formation od monazite
803 and allanite during contact and regional metamorphism of pelites: petrology and geochronology.
804 Contributions to Mineralogy and Petrology, 145, 228–250. http://www.dx.doi.org/10.1007/s00410-
805 003-0446-1.

806

807 Wu, C.M., 2015. Revised empirical garnet-biotite-muscovite-plagioclase (GBMP) geobarometer in
808 metapelites. Journal of Metamorphic Geology, 33, 167–176. http://dx.doi.org/10.1111/jmg.12115.
809
810 Zenk, M. and Schulz, B., 2004. Zoned Ca-amphiboles and related P-T evolution in metabasites
811 from the classical Barrovian metamorphic zones in Scotland. Mineralogical Magazine, 68/5, 769–
812 786. http://dx.doi.org/10.1180/0026461046850218
813
814
815 **Supplementary Files**
816
817 **Figure S1:** (a) Geological map of the area W of Franz-Senn-Hütte, Alpeiner Valley, Austroalpine
818 Oetztal-Stubai basement. (b) Lithological cross section.
819
820 **Table S2:** Electron microprobe analyses of Ca-amphiboles in amphibolitized eclogite and
821 amphibolite from the Alpeiner Valley around Franz-Senn-Hütte, Austroalpine Oetztal-Stubai
822 basement. Cation formula is calculated on the basis of 23 oxygens (Leake et al.,1997), with site
823 allotment CNK13.
824
825
826
827 **Captions**
828
829 **Figure 1:** (a) Location of study area in the basement units of the Central and Eastern Alps: BSTW
830 - Basement South of Tauern Window; GWZ - Graywacke Zone; IL - Insubric Line; IQ - Innsbrucker
831 Quartzphyllite; JL - Judicarie Line; Ko - Koralpe; Oe - Oetztal-Stubai; PL - Periadriatic Lineament;
832 Sa - Saualpe; SA - South Alpine; Si - Silvretta; TW - Tauern Window (Penninic Unit). (b)
833 Geological map of the Oetztal-Stubai basement in the Central Alps, with Variscan mineral zones
834 after Purtscheller (1978), and domains of Alpine Cretaceous metamorphism after Thöni (1981) and
835 Hoinkes and Thöni (1993). Study area around the Franz-Senn-Hütte is marked.

836

837 **Figure 2:** (a) Geological sketch map of the area W of Franz-Senn-Hütte in the Alpeiner Valley,
838 Austroalpine Oetztal-Stubai basement, with sampling locations referred to in the text. See details in
839 Fig. S1.

840

841 **Figure 3:** (a) Map of energy dispersive X-ray (EDX) spectra in garnet micaschist. Spectra for
842 garnet porphyroblasts are labelled in a generic way by Fe, Mg, Mn, and Ca contents in normalised
843 element wt%. Bt - biotite; Grt - garnet; Locations of analytical profiles and traces of foliations S_1i
844 and S_2 are marked. Numbers are EMP analyses along profiles. (b, c) Zonations in micaschist
845 garnet including almandine (Alm-50 %, due to scale), pyrope (Prp), grossular (Grs) and
846 spessartine (Sps) components (in mole %). Numbers are selected garnet analyses used for
847 geothermobarometry. The profiles are labelled from the cores (c) to the rims (r) of garnet. (d)
848 Garnet zonations in *X*Mg-*X*Ca coordinates. Arrows indicate core-to-rim (c, r) zonation trends from
849 single garnet profiles. Numbers are selected garnet analyses for geothermobarometry. The garnet
850 *X*Mg-*X*Ca zonations refer to the semiquantitative pressure-temperature trends A (heating-
851 compression), B (heating-decompression) and C (isothermal decompression), as outlined in Spear
852 (1993). (e) Mineral chemistry and zonations of Ca-amphibole in metabasite samples, according to
853 Leake et al. (1997). (f) Ca-amphibole zonations in ^{IV}Al vs ^{VI}Al coordinates, with relative *P-T* trend.
854 c1, c2 - cores, r1, r2 - rims of amphiboles.

855

856 **Figure 4:** (a) Geothermobarometry and *P-T* estimates from garnet micaschists. Crosses mark
857 results from garnet-biotite (Grt-Bt) thermometers and GASP and GBMP barometers (HP - Holland
858 and Powell (1998); SK - Spear and Kohn (1999); Wu - Wu (2015). See text and Table 1 for details
859 and combination of analyses. Arrow indicate P-T trend given by combination of data from samples
860 RZ33 and RZ42. The aluminosilicates (And, Ky, Sill), cordierite-in (Cd+), muscovite-out (Ms-) and
861 staurolite-in and -out (Sta+, Sta-) univariant lines are after Spear (1993). Bold cross at lower right
862 marks a general uncertainty of ± 50 °C/1.0 kbar. (b) Geothermobarometry and P-T estimates
863 (crosses) from amphibolitized eclogite (RZ24) and amphibolite (RZ37), by the Ca-amphibole
864 equilibria geothermobarometer (ZS) by Zenk and Schulz (2004). Isopleths for jadeite (Jd10)

865 content in clinopyroxene after Holland (1980; 1983). The arrow combines the *P-T* data from garnet
866 micaschists to data from metabasites.
867
868 **Figure 5:** Microstructures of monazite in backscattered electron images (BSE). Numbers are
869 single Th-U-Pb ages in Ma. Weighted averages with 2 sigma error are calculated from several
870 analyses within a grain. (a) Large monazite (Mnz) with slightly embayed rims and patchy darker
871 core zones, with Permian and Triassic ages. (b) Large monazite with patchy darker core zone. (c)
872 Embayed large monazite with darker domains and numerous Mesozoic single ages. (d) Initial
873 stage of corona structure around a Carboniferous-to-Permian monazite with apatite (Ap) and
874 allanite (Aln) along the margin. (e) Progressed stage of corona formation with broad apatite zones;
875 weighted average ages are Triassic. (f) Late stage of corona formation with broad apatite and
876 allanite rims and thin relic monazite with Triassic ages. (g) Large cluster of small monazite grains
877 which are surrounded by allanite. (h, i) Details of monazite cluster arrangement with allanite rims
878 around all small monazite grains. The monazite cluster is embedded in coarse-grained matrix with
879 biotite (Bt), plagioclase (Pl) and quartz (Qtz).
880
881 **Figure 6:** Mineral chemistry of monazite and distributions of monazite Th-U-Pb chemical ages. (a,
882 b) Monazite mineral chemistry vs age for each sample. (c) Monazite LREE and HREE
883 compositions in mole fractions. (d) Diagram *X*GdPO4 vs *X*YPO_4, with compositions above the
884 garnet (Grt) metamorphic mineral zone as defined by Pyle et al. (2001). Moles calculated
885 according to Pyle et al. (2001). (e) Monazite compositions in reference to the cheralite substitution
886 trend, note different trends in samples RZ29 and RZ31. (f) Histogram with distribution of single
887 monazite ages to Permian (280 - 270 Ma.) and Triassic (220 - 210 Ma) populations.
888
889 **Figure 7:** Th-U-Pb chemical model ages of monazite (Mnz). Total ThO_2* vs PbO (wt.%) isochrons
890 diagrams. ThO_2* is ThO_2 + UO_2 equivalents expressed as ThO_2. General minimal 2σ error on
891 monazite PbO analysis is shown by a bar. Regression lines with the coefficient of determination R^2
892 are forced through zero (Suzuki et al., 1994; Montel et al., 1996). Weighted average ages (Ma)
893 with MSWD and minimal error of 2σ are calculated from single analyses according to Ludwig

(2001). The symbols mark analyses belonging to monazite age populations and defining isochrones, falling into Carboniferous, Permian and Triassic ranges of ages.

Figure 8: (a) P-T-t evolution and monazite ages in the Stubai region (Alpeiner Valley), compared to data from the Oetztal basement to the west, given in Rode et al. (2012). Segments of the P-T path are marked with EMP monazite ages, and data from eclogites in Miller and Thöni (1995). Stability fields for kyanite (Ky), andalusite (And), sillimanite (Sil) after Spear (1993). stability fields of monazite (Mnz) and allanite (Aln) at different bulk rock contents as a function of Ca wt %, and with the xenotime (Xtm+) stability field (Janots et al., 2007; Spear, 2010).
(b) Frequency distribution (recalculated to percent) of the EMP-Th-U-Pb monazite ages in Stubai (Alpeiner Valley) as reported in Fig. 5f, compared to data from the Oetztal regions to the W, as reported in Rode et al. (2012).

Table 1: Electron microprobe analyses (wt.%, p.f.u.) of garnet (Grt), biotite (Bt), muscovite (Ms) and plagioclase (Pl) in micaschists and gneisses from the Austroalpine Oetztal-Stubai basement, Alpeiner Valley around Franz-Senn-Hütte, normalized to 12 oxygen (garnet), 11 oxygen (biotite, muscovite) and 8 oxygen (plagioclase). Almandine (Alm), anorthite (An), grossular (Grs), pyrope (Prp), spessartine (Sps) contents in mole %. Mineral analyses combined for geothermobarometric calculations are as follows: Sample RZ33: Grt31–Bt119–Pl73; Grt4–Bt108–Pl170: Sample RZ42: Grt245–Bt161–Ms187–Pl171; Grt104–Bt161–Ms187–Pl171; Grt84–Bt247–Ms187–Pl203; Grt77–Bt247–Ms187–Pl203.

Table 2: Electron microprobe analyses of metamorphic monazite from metapelites of the Oetztal-Stubai basement in the Alpeiner Valley around Franz-Senn-Hütte. Th* is calculated from Th and U after Suzuki et al. (1994). Monazite ages from single analyses are given with 2sigma error. Mnz monazite single grain; Data from reference standard monazite Madmon (Schulz and Schüssler, 2013) is weighted average of 18 single analyses performed during the sessions on the samples.

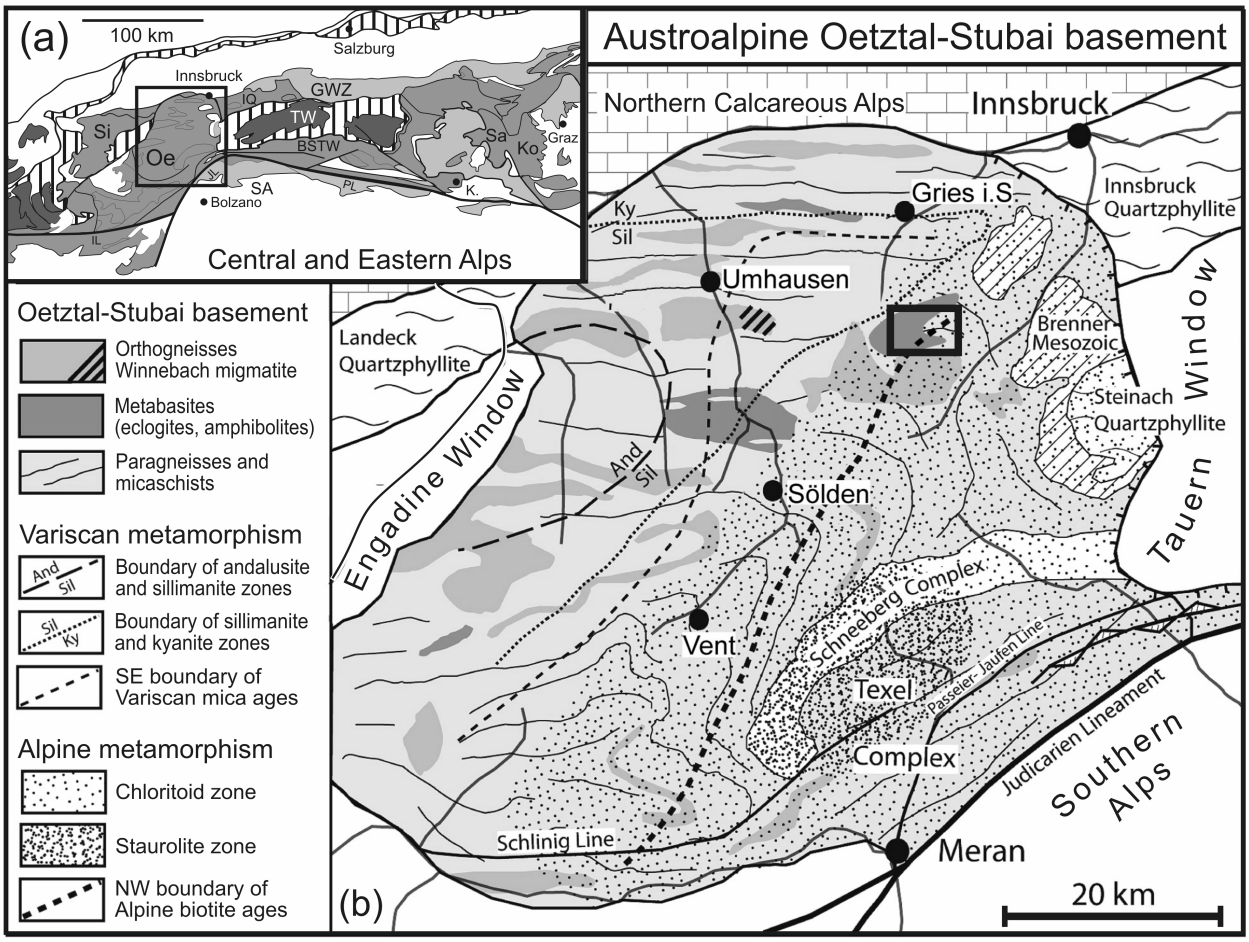

Schulz-Zimmermann-Fig 1

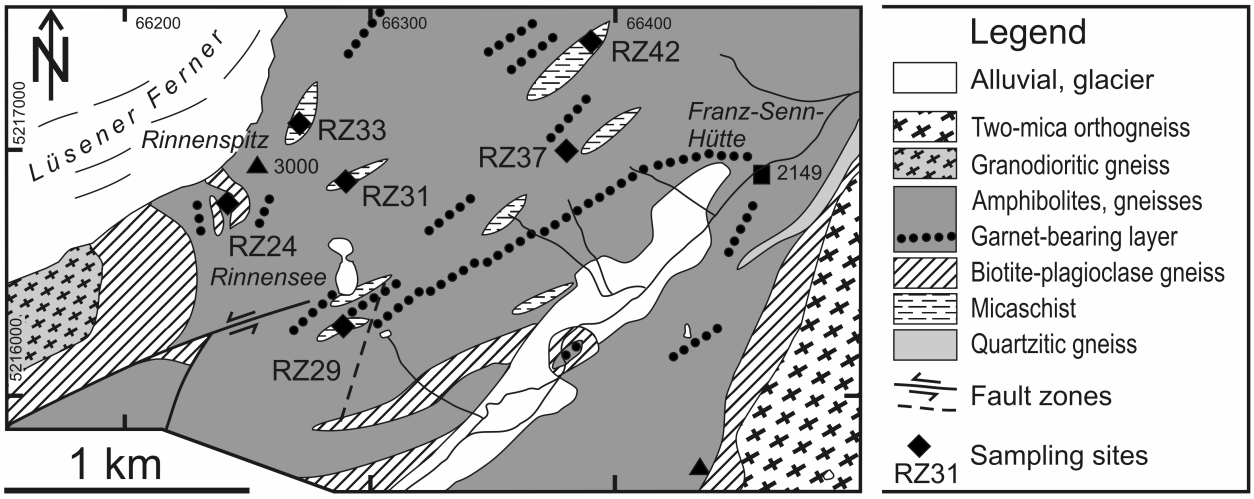

Schulz-Zimmermann-Fig 2

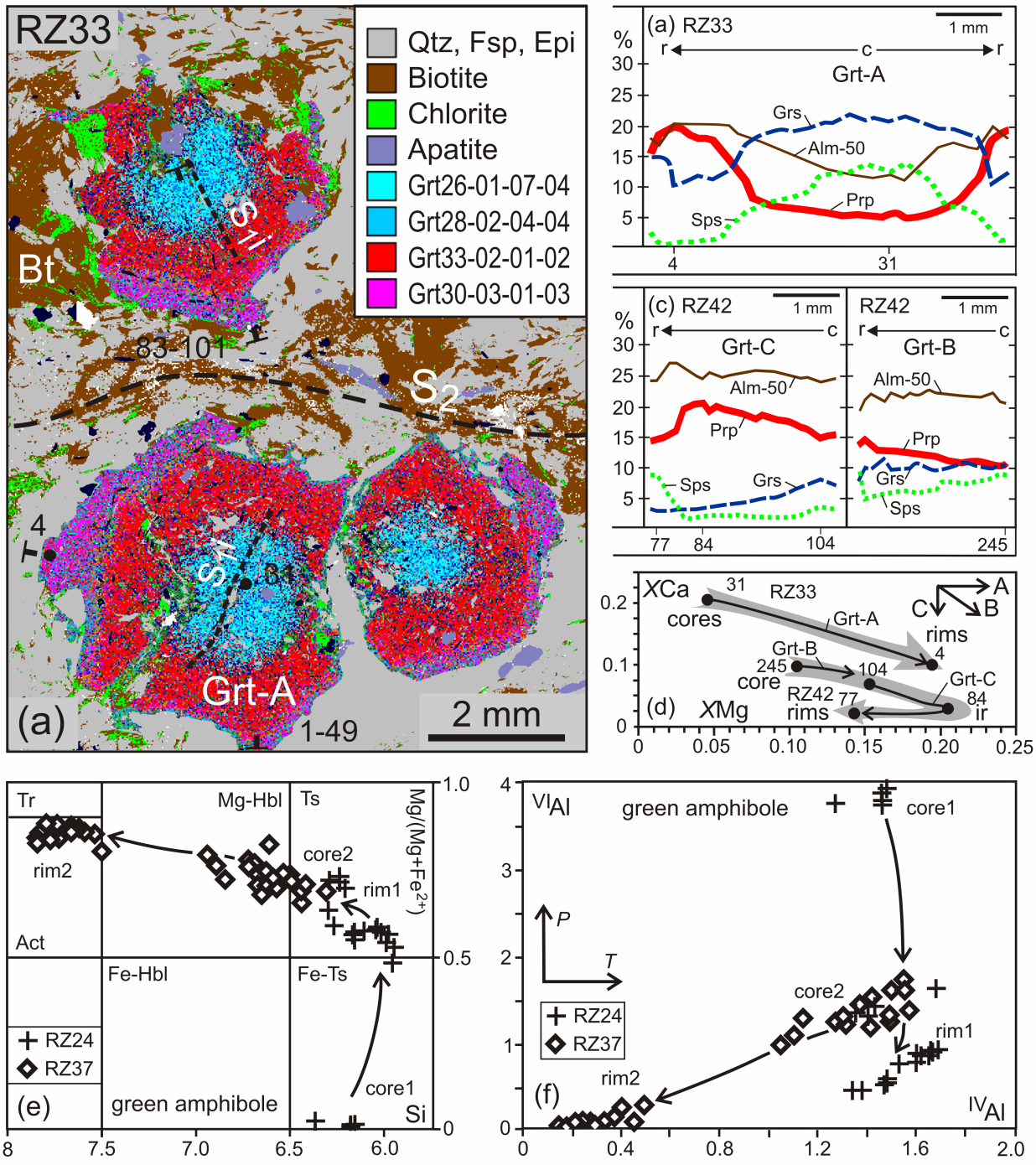

Schulz-Zimmermann-Fig 3 - online

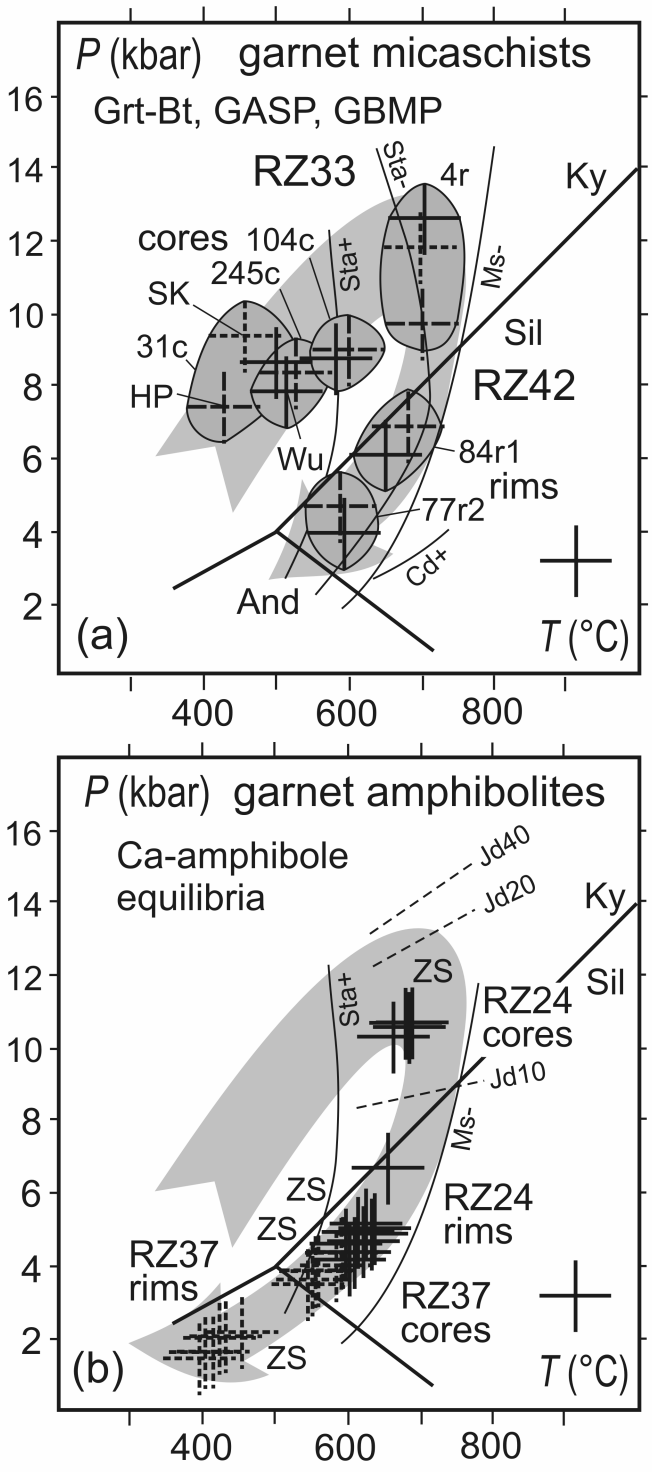

Schulz-Zimmermann-Fig 4

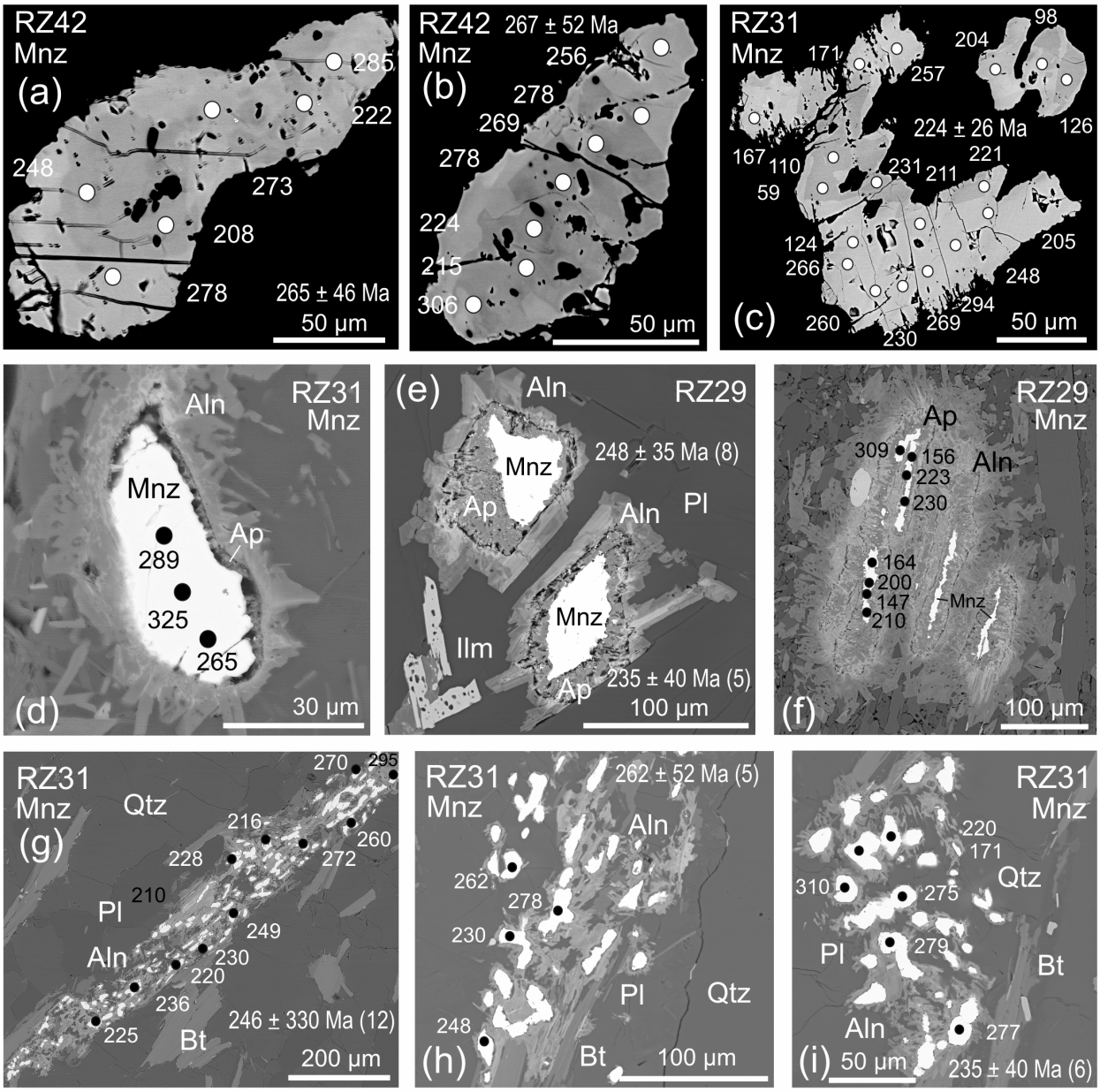

Schulz-Zimmermann-Fig5

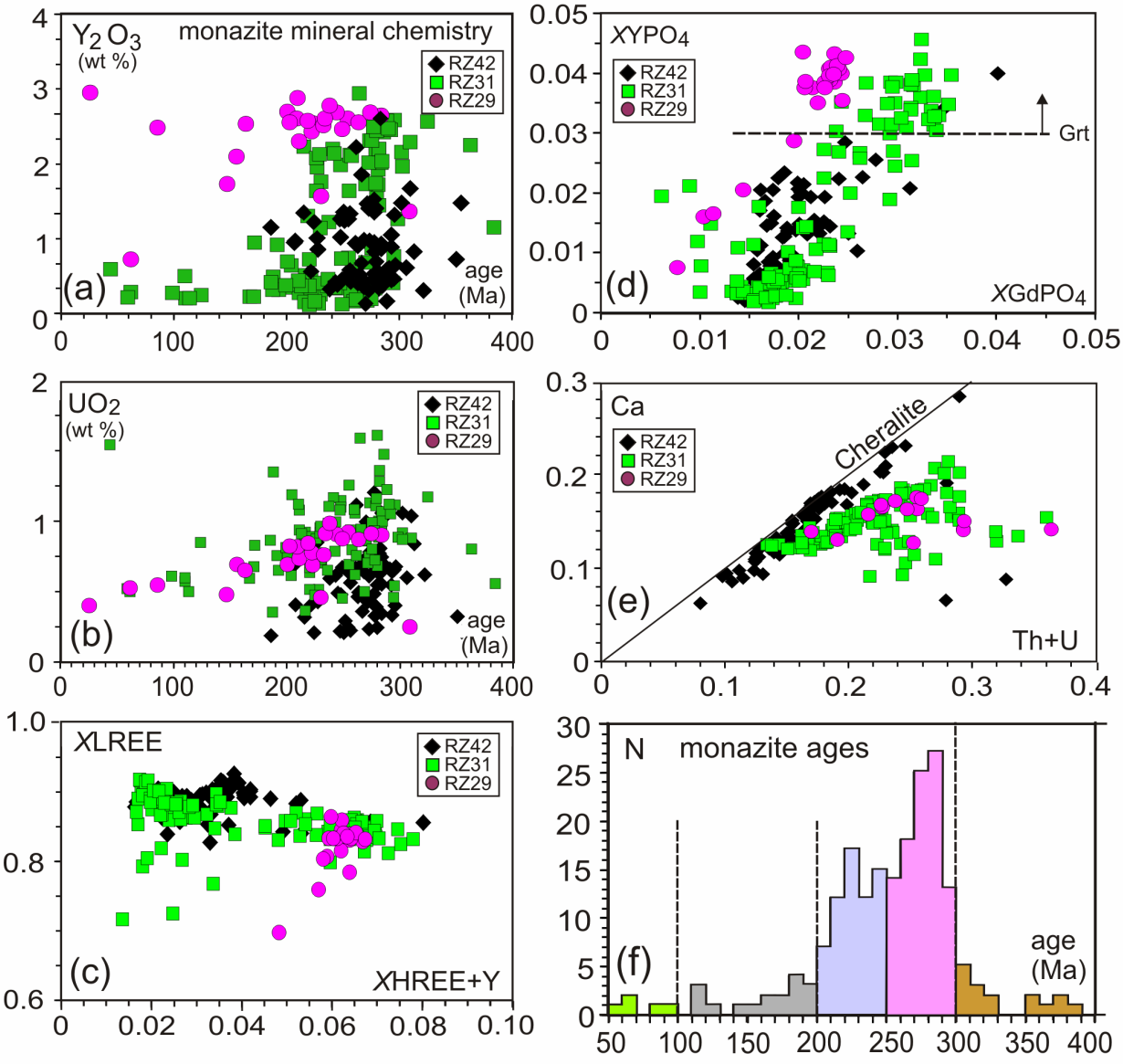

Schulz-Zimmermann-Fig6

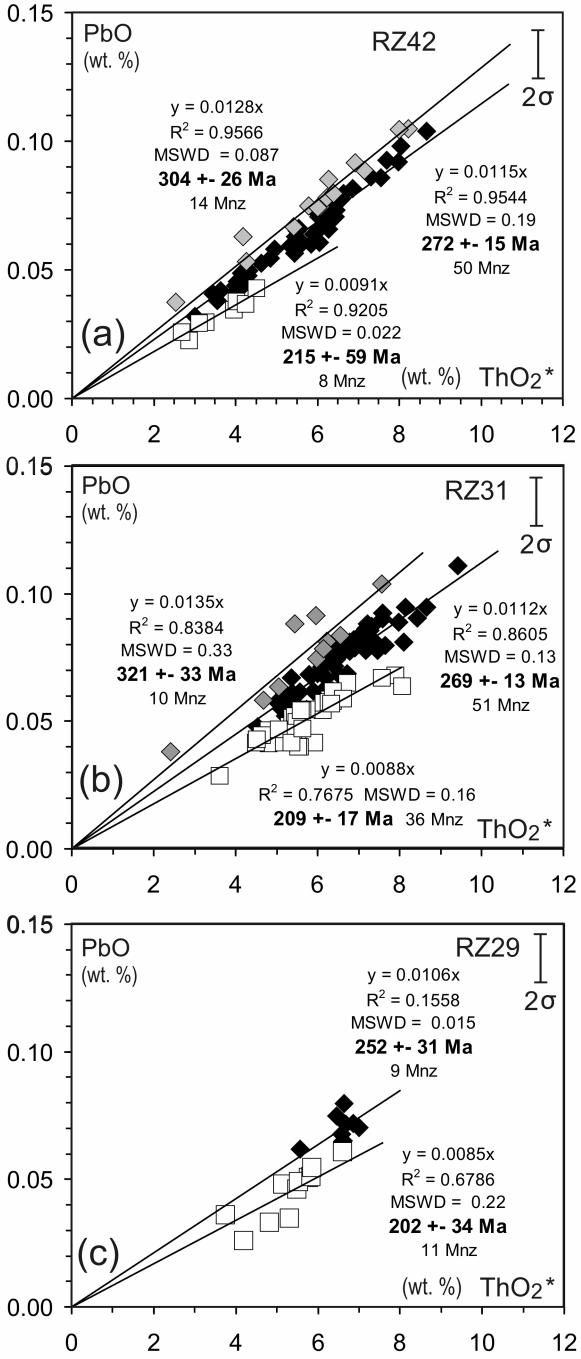

Schulz-Zimmermann-Fig7

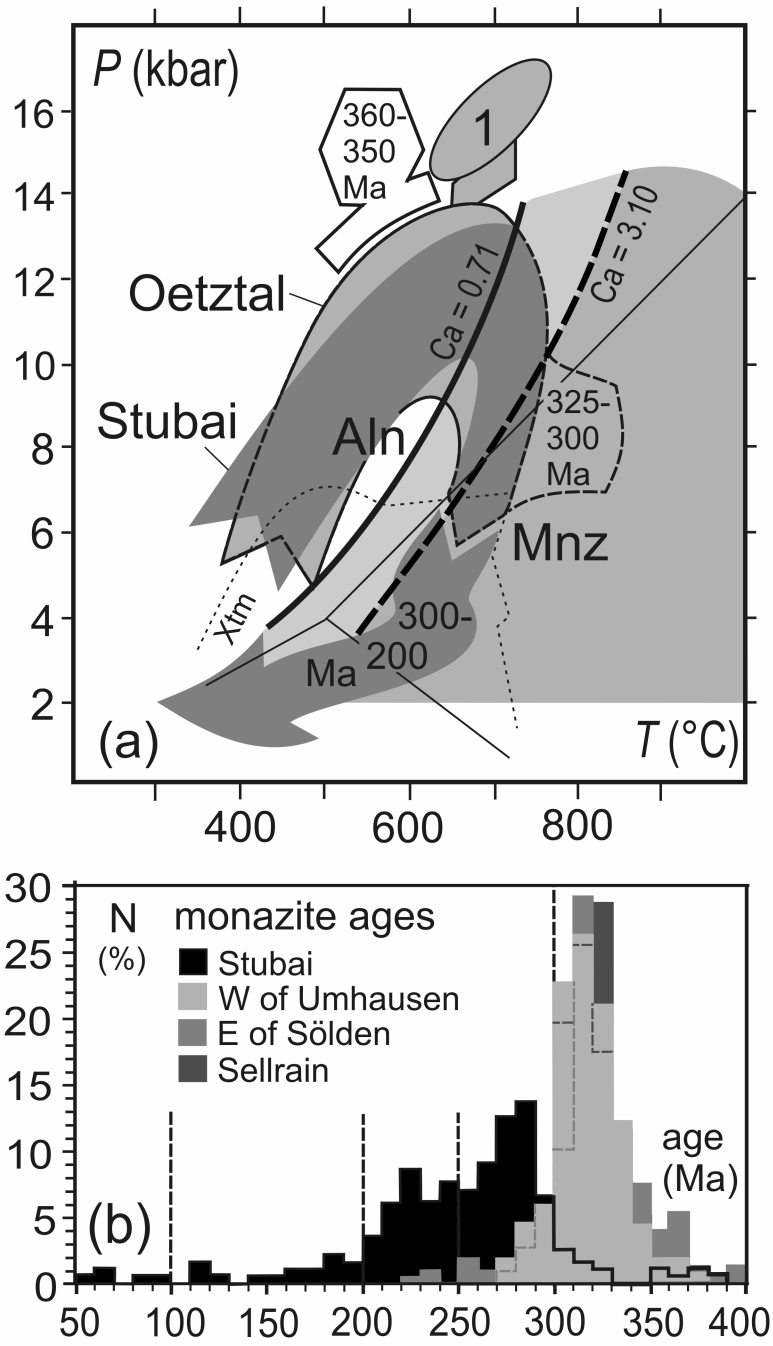

Schulz-Zimmermann-Fig8

	RZ33	RZ33	RZ42	RZ42	RZ42	RZ42
Grt	31c	4r	245c	104c	84r	77r
Si	3.013	2.972	2.997	3.004	3.003	3.000
Al	1.922	1.969	1.979	1.987	1.978	1.970
Fe	1.876	2.165	2.132	2.232	2.248	2.251
Mn	0.404	0.013	0.266	0.090	0.056	0.267
Mg	0.148	0.604	0.318	0.459	0.618	0.432
Ca	0.642	0.310	0.305	0.216	0.104	0.086
Tot	8.005	8.033	7.997	7.989	8.007	8.007
Alm	61.1	70.0	70.6	74.5	74.3	74.2
Prp	4.8	19.5	10.5	15.3	20.4	14.2
Sps	13.2	0.4	8.8	3.0	1.9	8.8
Grs	20.9	10.0	10.1	7.2	3.4	2.8
*X*Mg	0.048	0.195	0.105	0.153	0.204	0.142
*X*Ca	0.209	0.100	0.101	0.072	0.034	0.028
	Bt119	Bt108	Bt161	Ms187	Bt247	Ms188
Si	2.727	2.737	2.636	3.152	2.654	3.300
^{IV}Al	1.273	1.263	1.364	0.848	1.346	0.700
^{VI}Al	0.349	0.368	0.419	1.821	0.387	1.793
Ti	0.095	0.090	0.045	0.008	0.095	0.013
Fe	1.261	1.183	1.155	0.092	1.229	0.094
Mn	0.003	0.003	0.005	0.001	0.005	0.001
Mg	1.186	1.240	1.443	0.096	1.255	0.089
Ca	0.000	0.000	0.002	0.001	0.001	0.002
Na	0.024	0.028	0.027	0.131	0.030	0.128
K	0.922	0.919	0.692	0.839	0.793	0.770
Tot	7.840	7.831	7.787	6.990	7.796	6.890
XMg	0.48	0.51	0.56	0.51	0.51	0.49
Pl	173	170	171	173	203	204
Si	2.731	2.747	2.847	2.842	2.779	2.805
Al	1.254	1.239	1.150	1.152	1.220	1.190
Ca	0.279	0.260	0.152	0.163	0.222	0.205
Na	0.748	0.766	0.846	0.846	0.762	0.798
K	0.004	0.004	0.008	0.002	0.013	0.004
Tot	5.016	5.016	5.003	5.005	4.996	5.001
An	27.1	25.3	15.1	16.1	22.3	20.3

Schulz-Zimmermann-Table 1

Table 2

Sample	SiO_2	P_2O_5	CaO	Y_2O_3	La_2O_3	Ce_2O_3	Pr_2O_3	Nd_2O_3	Sm_2O_3	Gd_2O_3	ThO_2	UO_2	PbO	Total	Th	U	Pb	ThO_2*	Age	± 2σ
RZ29-4	0.34	30.29	19.01	1.17	9.61	19.85	2.62	9.85	1.77	1.30	2.27	0.456	0.036	99.02	1.99	0.402	0.034	3.740	230	164
RZ29-8	0.15	29.50	1.75	2.16	12.87	27.76	3.52	13.75	2.60	1.89	3.14	0.816	0.051	100.56	2.76	0.720	0.047	5.770	210	106
RZ29-m2-1	0.13	29.68	1.35	1.95	12.67	27.47	3.46	13.76	2.55	1.91	3.70	0.920	0.071	100.25	3.25	0.811	0.066	6.671	254	92
RZ29-m2-10	0.16	29.51	1.51	1.89	12.99	27.39	3.41	13.54	2.47	1.78	4.15	0.762	0.065	100.25	3.64	0.672	0.060	6.607	233	93
RZ29-m2-11	0.16	29.77	1.35	1.93	12.83	27.47	3.51	13.66	2.60	1.81	3.87	0.846	0.061	100.49	3.40	0.746	0.056	6.596	219	93
RZ29-m2-9	0.20	29.68	1.29	2.01	12.61	27.34	3.53	13.94	2.65	1.87	3.51	0.911	0.075	100.28	3.09	0.803	0.069	6.462	274	95
RZ31-m1-12	0.21	29.61	1.33	1.68	12.58	28.04	3.19	12.72	2.61	2.30	3.35	0.802	0.091	99.15	2.94	0.707	0.085	5.963	363	103
RZ31-m1-13	0.69	29.42	2.48	1.62	12.60	27.06	3.03	12.23	2.40	2.10	3.59	0.915	0.084	98.81	3.15	0.806	0.078	6.554	302	94
RZ31-m1-4	0.15	28.48	1.66	0.34	12.74	29.07	3.24	12.96	2.40	1.57	3.42	0.888	0.059	97.60	3.01	0.783	0.054	6.287	221	98
RZ31-m1-5	0.13	29.69	0.92	0.54	13.33	30.01	3.49	13.92	2.78	1.80	2.75	0.635	0.044	100.68	2.42	0.560	0.041	4.803	220	128
RZ31-m1-6	0.17	29.43	1.12	1.17	12.98	28.42	3.22	12.95	2.73	2.29	3.57	0.684	0.068	99.46	3.14	0.603	0.064	5.788	280	106
RZ31-m1-7	0.15	29.43	1.32	1.44	12.71	28.13	3.11	12.74	2.80	2.26	3.81	0.998	0.083	99.72	3.34	0.879	0.078	7.037	281	87
RZ31-m1-8	0.17	29.34	1.43	1.49	12.45	27.43	3.14	12.70	2.77	2.38	3.94	1.146	0.080	99.27	3.46	1.011	0.074	7.644	248	80
RZ31-m10-12	0.34	29.31	1.12	0.85	13.82	29.17	3.47	13.31	2.45	1.55	3.28	0.961	0.062	100.33	2.88	0.847	0.057	6.380	230	96
RZ31-m10-13	0.34	29.17	0.89	0.09	14.52	30.67	3.52	14.10	2.40	1.33	2.85	0.514	0.042	100.89	2.50	0.453	0.039	4.503	220	136
RZ31-m12-4	0.13	29.61	1.23	1.72	12.87	28.40	3.41	13.53	2.51	1.90	3.36	0.881	0.081	100.23	2.95	0.777	0.076	6.219	310	99
RZ31-m12-6	0.27	29.66	1.24	1.31	12.81	28.54	3.44	13.77	2.58	1.88	3.32	1.163	0.083	100.73	2.92	1.025	0.077	7.087	279	87
RZ31-m14-1	0.13	29.71	1.34	1.48	13.47	28.70	3.41	12.87	2.29	1.86	3.32	0.871	0.078	100.14	2.92	0.767	0.073	6.146	303	100
RZ31-m4-19	0.19	29.38	1.54	0.21	13.53	29.44	3.39	13.03	2.42	1.41	4.22	0.915	0.078	100.37	3.71	0.806	0.072	7.181	257	85
RZ31-m5-4	0.26	29.92	1.49	1.85	12.51	27.45	3.25	12.76	2.60	2.27	3.31	1.068	0.081	99.54	2.91	0.941	0.075	6.774	284	91
RZ31-m9-2	0.20	29.40	1.47	1.59	12.74	27.92	3.40	13.66	2.81	2.39	2.67	0.919	0.054	99.98	2.35	0.810	0.051	5.636	229	109
RZ42-m1-1	0.21	29.50	1.05	0.46	14.18	29.25	3.63	14.38	2.58	1.54	3.94	0.660	0.075	101.46	3.46	0.582	6.077	0.069	291	101
RZ42-m1-2	0.20	29.32	0.88	1.02	14.27	29.45	3.73	14.15	2.54	1.58	3.46	0.210	0.044	100.85	3.04	0.185	4.136	0.041	251	148
RZ42-m10-3	0.17	29.40	1.11	0.65	14.00	28.93	3.48	14.32	2.62	1.65	4.22	0.553	0.072	101.17	2.47	0.408	4.309	0.044	284	102
RZ42-m10-4	0.28	29.14	1.43	0.25	14.17	29.17	3.57	14.09	2.61	1.44	4.13	0.593	0.061	100.93	5.30	0.345	7.304	0.080	238	102
RZ42-m12-4	0.18	29.24	0.84	1.01	14.22	28.65	3.52	13.81	2.94	2.45	2.18	1.202	0.071	100.32	2.97	0.199	4.112	0.041	278	101
RZ42-m13-11	0.22	29.11	0.91	0.38	14.44	29.72	3.64	14.14	2.51	1.35	3.56	0.640	0.060	100.67	3.62	0.605	6.346	0.071	255	109
RZ42-m13-12	0.27	29.31	1.04	0.23	14.38	29.23	3.64	14.26	2.60	1.41	4.26	0.619	0.085	101.33	3.71	0.488	6.009	0.067	322	98
RZ42-m13-8	0.13	29.29	1.20	0.62	14.00	28.73	3.59	13.98	2.47	1.46	4.20	0.837	0.092	100.62	3.63	0.523	6.043	0.056	313	88
RZ42-m14ig2	0.25	29.27	1.36	1.11	12.92	27.70	3.48	13.57	2.65	2.08	4.79	1.056	0.105	100.34	1.15	0.375	2.687	0.024	302	75
RZ42-m15-3	0.18	29.39	1.34	0.12	14.24	29.20	3.53	13.69	2.39	1.09	4.62	1.054	0.098	100.96	1.92	1.060	6.072	0.066	289	76
RZ42-m4-4	0.12	29.38	0.83	0.68	14.74	30.06	3.65	14.20	2.65	1.56	2.81	0.462	0.048	101.19	3.13	0.564	5.628	0.056	263	142
RZ42-m5-1	0.26	29.18	1.46	0.52	13.68	28.46	3.55	13.49	2.43	1.24	6.04	0.391	0.086	100.79	3.74	0.545	6.271	0.079	279	84
RZ42-m6-1	0.26	29.17	0.97	0.46	15.08	29.62	3.61	13.67	2.39	1.38	3.85	0.599	0.075	101.13	3.70	0.738	6.924	0.085	306	106
RZ42-m7-1	0.26	29.10	1.03	0.36	14.49	29.25	3.62	13.91	2.54	1.40	4.12	0.687	0.077	100.83	4.06	0.929	8.039	0.091	287	97
Madmon-18	3.15	25.07	0.14	0.98	7.91	25.20	4.01	15.96	4.64	2.24	10.92	0.383	0.262	100.98	9.59	0.344	0.242	12.195	504	15

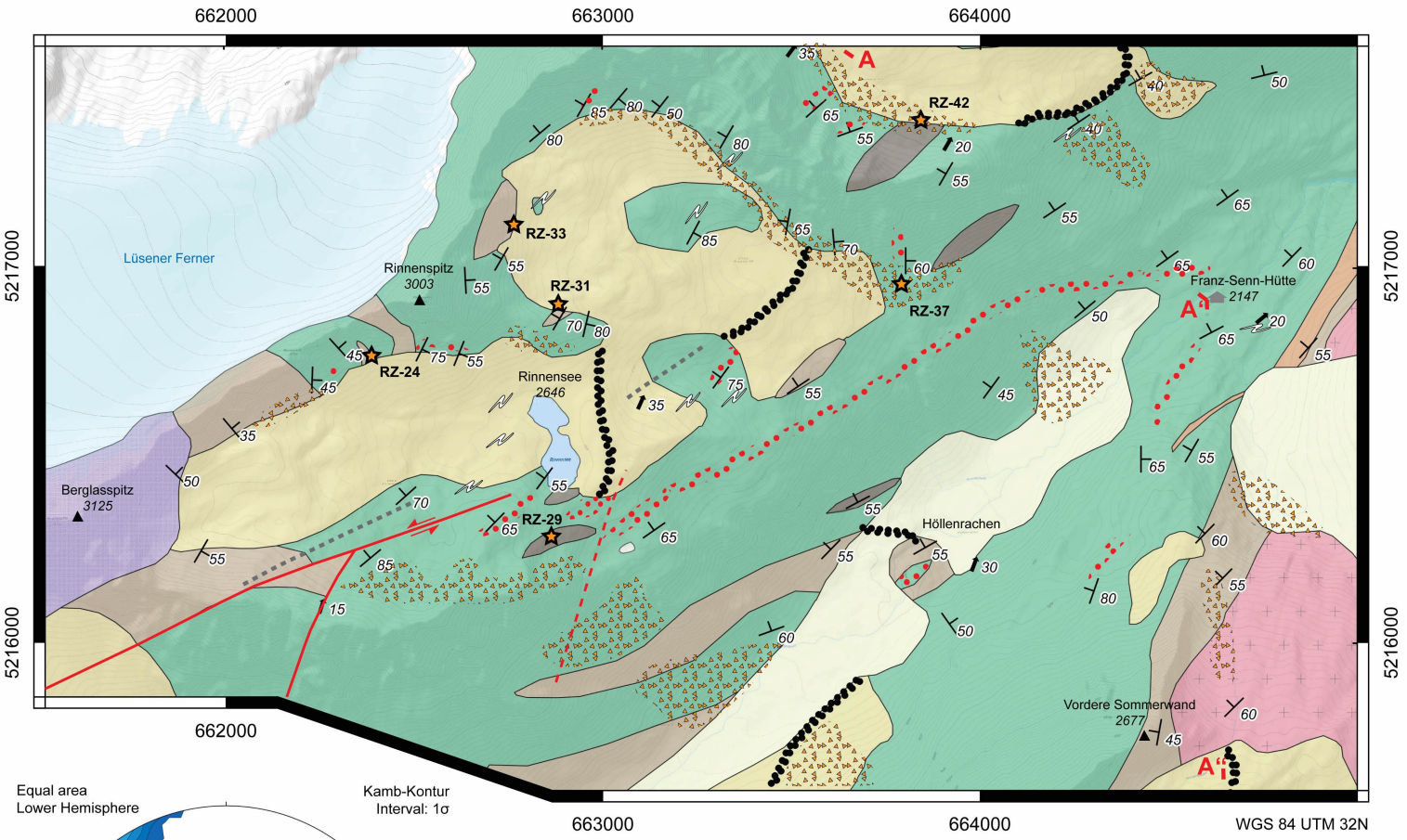

Legend

Quarternary

- Debris
- Alluvial terrace
- Moraine
- Frontal moraine

Austroalpine basement

- Quartz vein, partly mineralized

Granitoids

- Two-mica ortho gneiss
- Granodioritic gneiss

Units of CMBZ

- Amphibolites and gneisses, alternating
- Garnet-bearing layer
- Calc-silicate gneiss
- Biotite-plagioclase-gneiss
- Micaschist with garnet and staurolite
- Quartzitic gneiss

Tectonics

- Foliation (dip azimuth/dip)
- Fold axis
- Fault (inferred) with shear sense
- Fault (indicated)
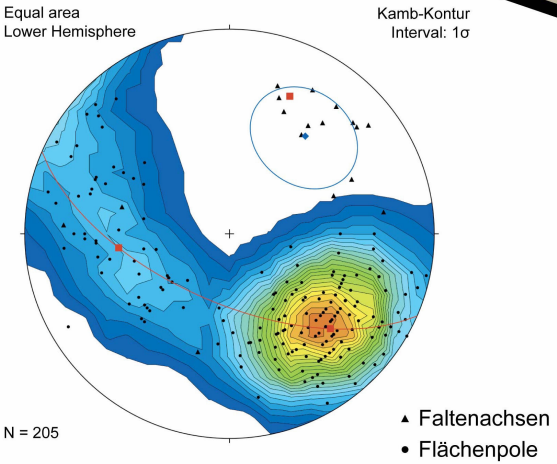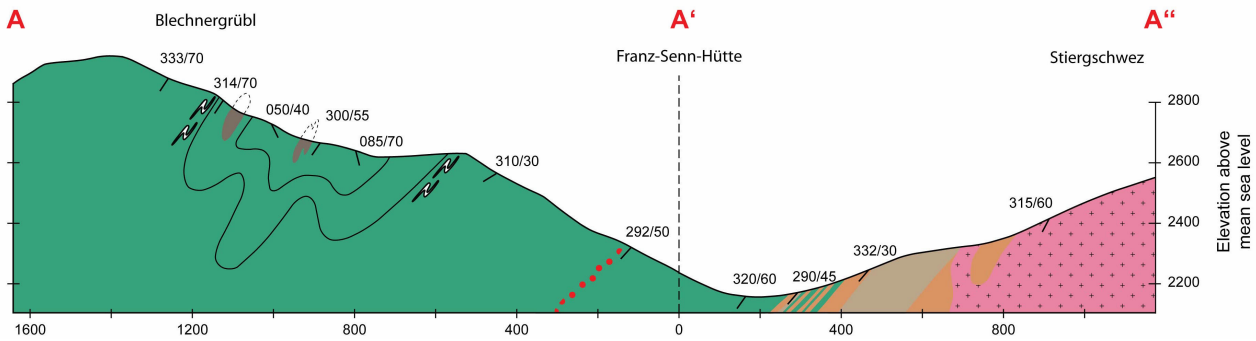
0 0,5 1,0
km